UNDERSTANDING & APPLICATION DRIVEN DESIGN OF METAL-ORGANIC FRAMEWORKS FOR CARBON CAPTURE

2^{nd} of July 2021
School of Basic Science
Laboratory of Molecular Simulation (LSMO)

École Polytechnique Fédérale de Lausanne

Nency Patricio Domingues

Prof. Berend Smit
Prof. Susana García
Fatma Pelin Kinik
Miriam Pougin
Dr. Christopher Ireland

Lausanne, EPFL, 2021

Acknowledgements

I would like to thank Prof. Berend Smit for giving me the opportunity to pursue my Master Thesis under his guidance and Prof. Susana García for her advises and with whom I had the opportunity to work with and collaborate in a common project.
I am deeply thankful to my mentors Pelin and Chris for their supervision, help and constant support throughout the thesis as well as Mish for the scientific discussions and for always bringing Peanut. I am also very glad for having shared the office, lunch breaks and ice-creams with the whole LSMO experimental group (Sam, Chris, Pelin, Bardiya and Mish) as well as Mohamed.
I am also very thankful to the whole LSMO computational group, especially to Miriam for all the computational calculations as well as to Sauradeep and Elias for the structure screenings. Moreover, I would also like to thank Pascal for his help and advises in complex Powder X-Ray Diffraction (PXRD) measurements.
And last but not least, I am very thankful to our secretary, Evelyn, for her administrative support and contagious smile.
I am also very thankful to LMER for their support and letting me perform the Thermal Gravimetric Analysis (TGA) as well as to LFIM, especially to Jordi for all the CO_2 and N_2 isotherms measurements as well as Ilia for being always available when I needed a chemical.

Sion, 2nd July 2021 N. D.

Abstract

CO_2 emissions have crucially contributed to climate change. Accordingly, several materials and processes have been developed for carbon capture. Metal-organic frameworks (MOFs) are novel porous materials which can be formed upon the assembly of organic linker(s) and metal components in a 1-, 2- or 3-dimensional periodic network. Thanks to their remarkable structural and functional tunability, including the variety of pore size and crystals shape, as well as the high surface area that can be attained, these materials have shown interesting performances for capturing CO_2.

To provide a better understanding of the interactions between MOFs and CO_2, we investigated a group of isostructural pyrene-based MOFs towards carbon capture in the first part of this thesis. For that matter, MOFs which possess the same ligand (i.e. TBAPy - 4,4',4",4"'-(1,3,6,8-pyrenetetrayl)tetrabenzoic acid) were studied further in detail and two different groups of TBAPy-based MOFs were designed with the intent to assess the influence of the: a) metal, and b) topology on the CO_2 adsorption capacity of these structures. Our investigation showed that depending on the metal used in the structure, the distance of the pyrene stacking in the TBAPy ligand is changing, resulting in different CO_2 adsorption capacities. The experiments on Al, Ga, In and Sc-TBAPy MOFs demonstrated that Al-TBAPy has the best performance among them due to the optimal inter atomic distances of the pyrene stacks (i.e. 6.65 Å), which is in good agreement with the theoretical predictions. This proves that the metal has a clear affect on the adsorption properties. Similarly, different topologies (constructed with Zn ions and pyrene ligands) were also found to be affecting the interactions between CO_2 molecules and the MOF. The size and shape of the pores largely affects the uptake: smaller pores allow for stronger MOF-CO_2 interactions and contribute to having a higher uptake at lower pressures. On the other hand, the pore volume of the MOF is the main factor to be consider at higher pressures, as it allows to accommodate a higher number of CO_2 molecules.

To fight climate change with carbon capture technologies, understanding the interactions of CO_2 with the MOF is not the only crucial aspect of this journey. It is of great importance to consider the process requirements before starting the synthesis of new structures. In

the second part of this thesis study, we investigated reported structures which have been computationally been found to be promising for wet-fuel gas applications. From a list of 15 (computational) promising structures, HAKSIY (i.e. from the Cambridge Crystallographic Data Centre (CCDC reference code)) was successfully synthesized. Even though simulations predicted an extremely high uptake (ca. 10 mmol/g at 1.2 bar), the experimental results showed a much lower performance (1.5 mmol/g at approximately the same pressure). This can be attributed to an overestimation of the performance of this material as computationally, a perfect crystallinity is assumed.

Contents

List of Figures

List of Tables

Nomenclature

MOF: metal-organic framework
CO_2: carbon dioxide CH_4: methane
N_2O: nitrous oxide
HFCs: hydrofluorocarbons
PFCs: perfluorocarbons
SF_6: sulphurhexafluoride
DFT: density functional theory
FF: force fields
H_2bct: 3,5-bis(4-carboxy-phenyl)-1,2,4-triazole
bib: 1,4-bis(imidazol-1-ylmethyl)benzene) (bib)
H_2bdc: terephthalic acid
H_3tzdc: 4H-1,2,4-triazole-3,5-dicarboxylic acid
H_2BPZ: 4,4-bipyrazole
H_4EBTC: 1,1'-ethynebenzene-3,3',5,5'-tetracarboxylic acid
H_2aze: azelaic acid
m-H_2BDC: isophthalic acid
H_2ispc: 3-(4-carboxyphenylsulfonyloxy)-4-methoxybenzoic acid
H_4bptc: biphenyl-2,2',5,5'-tetracarboxylic acid

1 Introduction

1.1 Climate Change & CO_2 Emissions

The GHGs, as defined in the Kyoto protocol in 2008, consist of carbon dioxide (CO_2), methane (CH_4), nitrous oxide (N_2O), hydrofluorocarbons (HFCs), perfluorocarbons (PFCs) and sulphur hexafluoride (SF_6) (UNFCCC 2008) [1]. Such gases, including water vapor, enhance the natural greenhouse effect of Earth, meaning that they are able to absorb the infrared radiation (IR) coming from the sun and trap it in the atmosphere in the form of heat. Such effect is defined as "global warming" and if it goes unlimited, it will cause a significant climate change, leading to several consequences whose effects are not negligible: a rise of the Earth's global temperature and of the sea levels, an increase of the ocean acidification, among others life-threatening weather events [2]–[4].

The largest emissions of the GHGs started to occur during the industrial revolution, in the 1750s [5]. The two gases which majorly contribute to global warming are CO_2 and CH_4, accounting for an overall concentration of 66.2% and 17% in 2016, respectively [6]. The CO_2 emissions derive from the combustion of fossil fuels, including coal, oil and natural gas, for electricity generation as well as industrial processes and transportation [7]–[10]. In 2018, the CO_2 emissions related to fossil fuel and land-use-related technologies contributed to approximately 74% of the overall GHGs emissions, which is why post-combustion carbon capture technologies have to be developed [11].

Given the rising levels of CO_2 in the atmosphere (Figure 1.1), there is an urgent need for novel sorbent materials and/or technologies for carbon capture. In fact, climate change and the increase of the greenhouse gases (GHGs) concentration in the atmosphere, of which CO_2 is the largest component [12], are facts which go hand in hand and a concern which needs to be assessed. For that matter, responsibility and taking action in a world that is desperate for help are crucial to mitigate the harmful effects that come with it.

Climate change is a pressing environmental issue which needs to be addressed. Strategies to overcome this problem or, at least, minimize it are being developed. Several pathways to

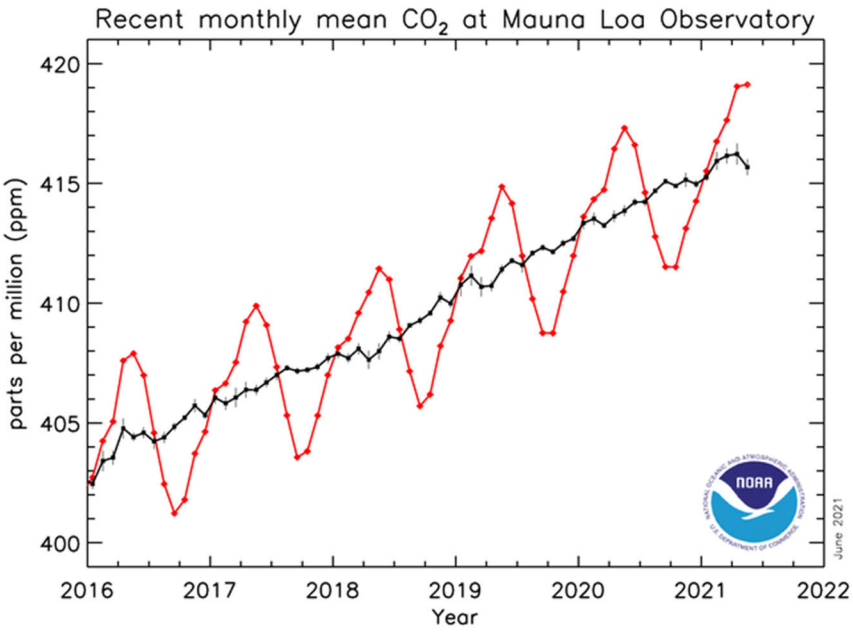

Figure 1.1 – Atmospheric CO_2 concentrations [ppm] throughout the years since 2016 until present, as recorded at the Manua Loa observatory in Hawaii [13].

reduce the CO_2 emissions exist and consist in the main categories cited hereafter [14], [15]: 1) increasing the energy efficiency of the current technologies and processes; 2) developing and using more sustainable technologies for the energy production (i.e. renewable energies such as: solar energy, biomass, wind and geothermal energy); 3) the use of carbon capture technologies and creation of CO_2 sinks for its sequestration.

In this thesis, we will be focusing on the very last point, particularly in the understanding, design and development of carbon capture materials to effectively adsorb CO_2.

1.2 Carbon Capture Technologies

Limiting the CO_2 emissions in the atmosphere is no small feat [16], [17] and several technologies to face and overcome this challenge are currently being developed. In this section, we will present the general classes that research groups worldwide have been investigating and can be applied at least at a pilot plant scale for post-combustion carbon capture [18]. Such technologies have been divided into two main categories: absorption and adsorption.

1.2.1 Absorption

Absorption consists of the complete dissolution of the compound of interest (i.e. absorbate) by the absorbent material, meaning that the substance enters the bulk of the material and

that the whole volume is engaged. Chemical and physical absorption processes can further be distinguished.

In the first one, a chemical reaction takes place and chemical bonds are created between absorbate and absorbent. The latter consists of a non-reactive mechanism where electrostatic or Van der Waals interactions occur [19].

1.2.1.1 Chemical Absorption Methods

Amines

Amine-based solvents are able of chemically interacting with CO_2 [20]. For that purpose, amine scrubing for CO_2 separation processes have been used in the gas-processing industry for several decades [21] and the most commonly employed agent is 20-30 wt% aqueous monoethanolamine (MEA), which was proposed in 1930 [14], [18].

The original process was developed by Bottoms [22] and consists of two columns: a packed absorber for the capture of CO_2 and a stripper for the solvent regeneration. At the very first stage of this process, fuel or combustion gas is introduced at the bottom of the absorber, while the aqueous amine solution flows in counter-flow direction, from the top to the bottom [23]. Thus, the CO_2 is absorbed into the amine aqueous solution at 40 °C and 1 bar. For the solvent regeneration and the re-use of the solution for several cycles, the amine solvent is regenerated by stripping with water vapor varying between 100 and 120 °C. The water vapor is then condensed while a stream of pure CO_2 can be compressed to 100 - 150 bar for geologic sequestration [22]. MEA is very appealing due to its commercial availability, relatively low price and its high reactivity and fast absorption process. However, it may degrade in oxidizing environments and be corrosive if used in high concentrations. This technique is also widely known by its intensive energy consumption during regeneration in the stripping section. All these disadvantages compromise this process to be used at larger scales [14], [20], [21].

Frequently used solvents can also be N-methyldiethanolamine (MDEA), as it shows a higher CO_2 loading capacity, corrosion resistance, degradation resistance and lower energy demand in the regeneration step than MEA. Similarly, di-2-propanolamine (DIPA) has been used for its higher corrosion resistance and lower energy costs but both solvents still present similar drawbacks as MEA [14], [24].

Other amine-based solvents can be used as CO_2 absorbents. For instance, secondary and tertiary amines have also been studied and the results show that sterically hindered amines (e.g. 2-amino-2-methyl-1-propanol (AMP)) allow for a more economic solvent regeneration as they give rise to a less stable carbamate upon CO_2 absorption than the primary amines and thus, to a higher absorption capacity [25]. Moreover, AMP also shows a higher selectivity, corrosion and degradation resistances than MEA [14], [23].

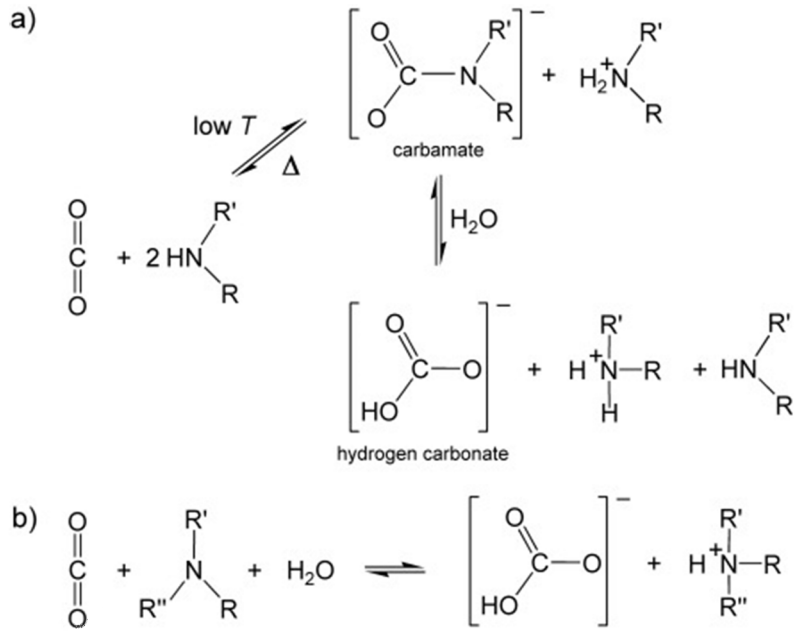

Figure 1.2 – Reaction schemes of the CO_2 absorption by a) primary or secondary and b) tertiary amine-based solvents [23].

Moreover, amine blends, which consist of a solution of at least two amine-based solvents with different ratios [24], are commonly used as absorbents. A very common mixture is piperazine (PZ) and AMP. The advantage of such blends is that each compound tends to compensate the other solvent's characteristics. For instace, in this case, the steric hindrance of AMP can influence the mass transfer, which would reduce the rate of reaction, but PZ allows to overcome this issue as it has the ability to rapidly form carbamates with CO_2 [14], [18].

Ammonia

Ammonia-based (NH_3) wet scrubbing is a classical example and one of the most widely studied liquid-solid separation absorbents. Considering that this compound is in the gaseous state at room temperature, aqueous NH_3 consists of an aqueous solution of this gas dissolved. Upon its reaction with CO_2, ammonium and bicarbonate are formed. These products are indeed in liquid and solid phases, which allows for an easier separation and absorption, thanks to the phase separation [18]. Such mechanism has the advantage of allowing for a greater CO_2 absorption capacity and lower energy consumption. Moreover, is is commercially available and allows for the removal of other species such as SO_2 and NO_2 [14], [18]. Moreover, it has the advantage of being thermally stable, resistant to oxidation, and has considerably lower energy requirements for the regeneration step [18]. The drawback of such technique consists mainly on ammonia's high volatility, and thus higher vapour pressures than other

systems. Lower temperatures have been studied to enhance the solubility of these gases, however the mass transfer rate is highly decreased, which leads to the formation of ammonium carbamate/bicarbonate precipitates [18], [26].

Potassium Carbonate
Aqueous potassium carbonate (K_2CO_3) has the advantage of being less volatile and more resistant to oxidative degradation compared to amines. However, considering it presents very low mass transfer rate, it is often combined with promoters (e.g. inorganic salts of arsenites, borates and silicates or amines and their derivatives) to overcome this issue [14], [18].

Ionic Liquids (ILs)
ILs may also be employed for carbon capture thanks to their very appealing properties: non-inflammability nor explosivity and very low vapor pressure due to their high boiling points [14]. Similarly to other types of solvents, ILs can also be combined with amines to take advantage of both compounds.

1.2.1.2 Physical Absorption Methods

Several processes which use different absorbents have been developed for physical absorption. A few examples of this type of absorption are: retisol, which operates with methanol (MeOH) as a solvent; selexol, which operates with dimethyl ether of polyethylene glycol (DMPEG) and purisol, which uses N-methyl-2-pyrrolidone (NMP). The common characteristic of all these processes is that no chemical reaction takes place between the absorbent and absorbed material, instead, electrostatic or Van der Waals interactions occur [27].

1.2.2 Adsorption

Adsorption can be described as the adhesion of a compound of interest (i.e. adsorbate) to the surface of the adsorbent material [19]. Different types of CO_2 adsorbents have been developed up to date, which will be summarized in the following sections.

Zeolites
Zeolites are porous crystalline aluminosilicate minerals, whose pores are of molecular dimensions, and their surface areas can range between 200 and 500 $m^2\ g^{-1}$ [18], [28]. Thanks to their advantageous characteristics, including the small pore size, high surface areas, tunable chemistry and flexibility of the structure, zeolites have been often employed in catalysis as well as separation processes. However, the low pore dimensions (channels < 0.8 nm and cavities < 1.5 nm), lead to diffusion problems and consequently, to high pressures in flow systems, which affects the employment of these materials at larger scale [28]. For that matter, solutions to overcome this issues have been developed by either increasing the pores dimensions to at least 1.5 nm, or decreasing the zeolite particles in order to reduce the diffusion path length. However, the pores sizes achieved were modest and it was observed that the efficiency of these materials in reacting with larger molecules was lower. Moreover, the reduction of the

particle size to less than 100 nm leads to less perfect crystals, lower pore volume as well as lower hydrothermal stability [28].

The SiO_2/Al_2O_3 ratio in the zeolite network has an influence in the properties of the structure: a higher ratio increases the thermal stability, while a lower one allows for strong interactions with the quadrupole moment of CO_2 molecules thanks to the presence of cations in the network [18], [23]. For that matter, the topology and composition of zeolites may widely influence the CO_2 adsorption capacity. For instance, if large, electropositive and polyvalent cations (e.g alkyl amines) are impregnated into their internal surfaces, the gas sorption properties of these materials can be increased.

Similarly to what was discussed in the single-amine absorbent section, primary amine-modified silica materials allow for more stable carbamate species formation and thus, promotes the adsorption of CO_2 [23]. On the other hand, zeolites are also widely known for their sensitivity to moisture and the competition between water and CO_2 for the binding sites in their structures. Such effects can lead to lowering the performances of these materials.

Zeolite 13X is a classical example of this class of materials and it is also often taken as a reference in CO_2 capture studies.

Carbon-based Materials
Carbon-based materials are mainly composed of carbon atoms. Several sub-classes can emerge: low-cost pyrogenic carbon materials, such as charcoal and biochar; activated-carbons and carbon nanomaterials, such as graphene and carbon nanotubes [18].

Physisorption is the main mechanism of adsorption for this type of materials, meaning that the interactions are mainly due to Van der Waals forces between CO_2 and the adsorbent [29]. To increase the CO_2 uptake, it is possible to insert functional groups containing oxygens, as they allow for chemical interactions between the CO_2 molecules and the adsorbent material [18], [29].

Metal-Organic Frameworks (MOFs)
Metal organic frameworks (MOFs) are porous materials consist on the assembly of organic linkers and metal components in a 1-, 2-, or 3-dimensional periodic network (Figure 1.3). These materials have the great advantage of being remarkably tunable which makes them suitable for a wide range of applications. For instance, they can be highly porous and be able to reach outstanding surface area values of over 6000 $m^2\ g^{-1}$. Their pores, as well as the size and shape of the crystals, can also be modulated depending on the interest and application. MOFs also allow for the introduction of functional groups (e.g. via the incorporation of polymers in the MOF structure, or the modification of ligands) to enhance and/or selectively interact with the adsorbate molecules (e.g. CO_2) [30]. All these characteristics and chemical diversity can be achieved by varying the starting materials (i.e metal salts, organic linkers and solvents) as well as the reaction conditions (i.e. modulators (pH of the reaction mixture), temperature, pressure and concentration) [30]. Thanks to their unique characteristics they have been widely used

for several applications, including gas separation/adsorption and storage as well as catalysis and photocatalysis (e.g. hydrogen evolution, H_2, CO_2 and N_2 reduction, etc.) [30], [31].

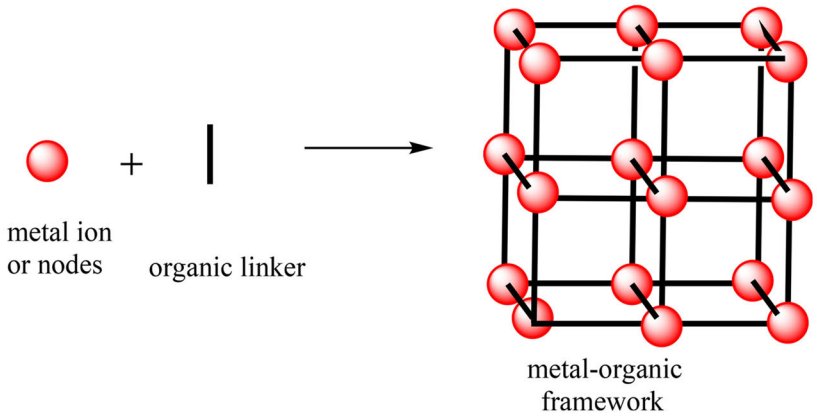

Figure 1.3 – Representation of a porous and crystalline MOF and its repeating structural units [31].

Due to the high energy demand and costs for CO_2 capture that some conventional methods (i.e. amine-based solvents absorption) present, as well as the lack of structural tunability of classes such as zeolites, activated carbons, etc., there has been an increasing interest to design and develop new materials for such application. Thanks to their outstanding chemical properties and morphological characteristics, MOFs are nowadays being extensively studied for the physisorption of CO_2 and have been showing promising results. Indeed, the highest amount of CO_2 captured by a MOF up to date corresponds to 74.2 wt% at 298 K and 5.0 MPa by MOF-210 (with a BET surface area = 6240 $m^2\ g^{-1}$) [30]. Besides the extremely high surface area, tunable and well-defined channels, as well as a network which presents a permanent porosity, MOFs can also be modified in order to have higher affinity for CO_2. Such properties can be developed by different methods [18], [30]:

1. **Open Metal Sites (OMS)**

   The creation of OMS corresponds to the removal of solvent molecules or water which are coordinated to the metal (Figure 1.4), meaning that the metal site will become coordinatively unsaturated. Such process usually occurs upon activation (temperature increase under dynamic vacuum). Some of the most widely known MOFs with OMS are HKUST-1 (HKUST-1: Hong Kong University Science and Technology) and M-MOF-74 (M = Mg, Mn, Fe, Co, Ni, Cu, Zn). Poloni et al. suggest that for a high CO_2 adsorption, one needs to consider the electronic configuration of the metal site (i.e. different metal substitutions) but also the bonding geometry [18], [30], [32].

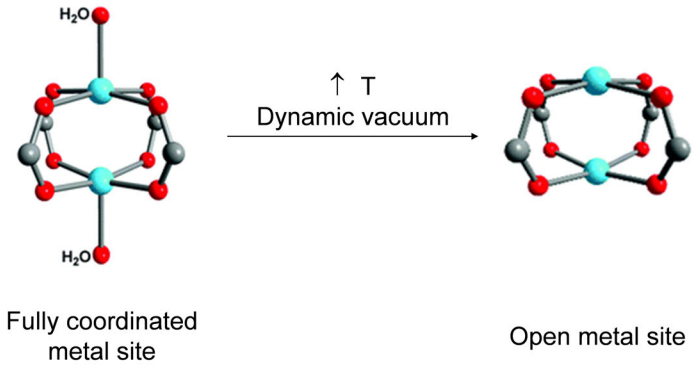

Figure 1.4 – Schematic representation of the formation of an open metal site in HKUST-1. Image adapted from [33].

2. **Ligand Functionalization**

   The insertion of functional groups in the organic linkers (Figure 1.5) used for the MOF synthesis can also increase the CO_2 adsorption capacity and selectivity compared to other gases. Considering that CO_2 has a very strong quadrupolar moment and other common gases (CH_4, H_2, N_2) are either non- or weakly polar, the introduction of polar functional groups in the MOF structure facilitates the adsorption of CO_2. Another approach would be to insert Lewis basic sites (e.g. amine groups (-NH_2)) which is able to interact with CO_2. However, this approach can lead to clustering of the functional groups and thus, lowering the CO_2 adsorption capacity [18], [30], [34].

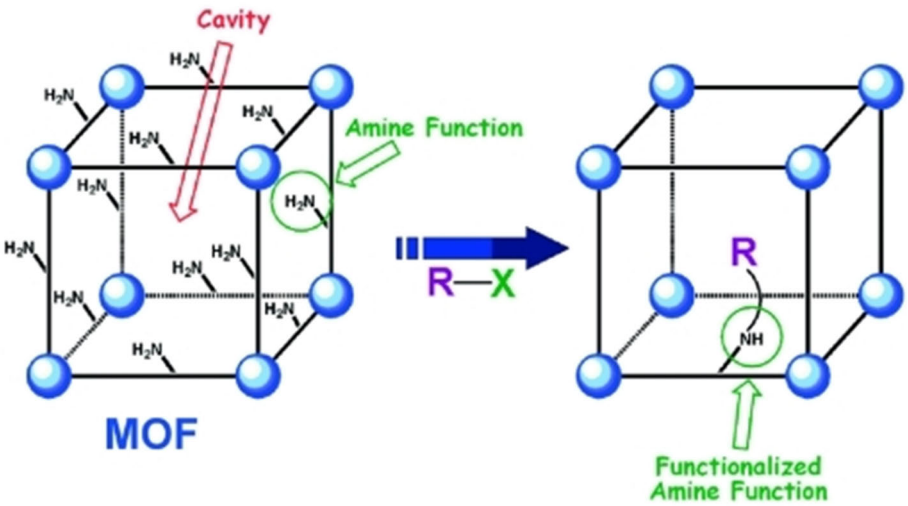

Figure 1.5 – Schematic representation of a ligand functionalization [34].

3. **"Breathing" Behaviour**

   The "breathing" property of certain structures corresponds to an irreversible structural transformation (i.e. expansion or contraction) upon adsorption/desorption (Figure 1.6).

Such phenomenon can have thus an influence on the pore shape and size, which can become narrower or larger depending on the MOF [18], [30], [35].

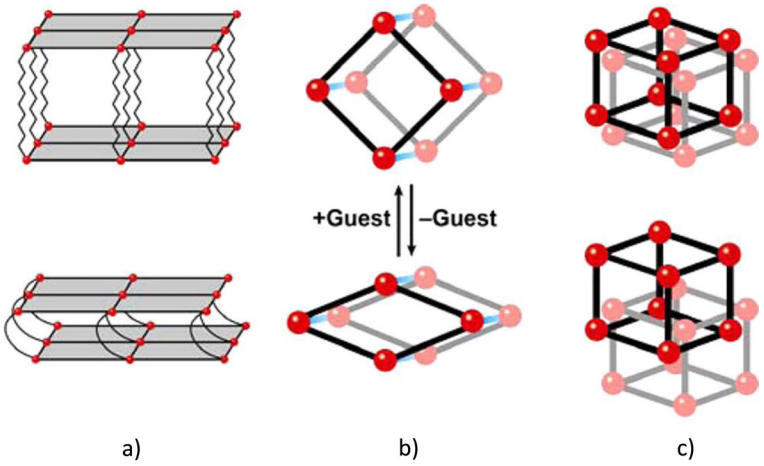

Figure 1.6 – Representation of the dynamic behaviour of a MOFs upon interaction with guest molecules in a) 2 dimensions, b) 1 dimention, c) 3 dimensions. Colour code: red spheres, metal; black lines, ligand [35].

4. **Interpenetration/Catenation**

   Interpenetration in the framework takes place when long organic ligands are used in the synthesis, which gives then rise to the self-assembly of at least two independent frameworks within each other (Figure 1.7). Even though this process contributes to lowering the MOF's porosity, it can increase the selectivity for certain gases due to narrower pore sizes [18], [30], [36].

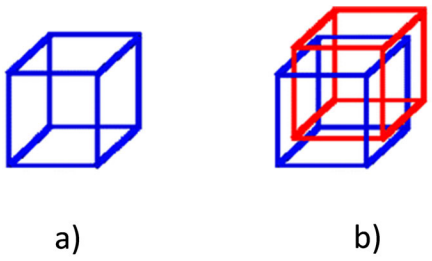

Figure 1.7 – Representation of a) non-concatenated MOF, b) 2-fold concatenated MOF [36].

Cyclic Adsorption Processes

To facilitate the use of adsorption materials for CO_2 capture at a large scale, cyclic adsorption processes have been developed for the regeneration steps of post-combustion capture. These processes can have different working principles: by total or partial pressure decrease (vacuum swing adsorption (VSA) and pressure swing adsorption (PSA), respectively) as well as by temperature increase (temperature swing adsorption (TSA)) [37].

- **Pressure/Vacuum Swing Adsorption (PSA/VSA)**

  PSA and VSA are technologies in which low temperatures and moderate pressures are used. Higher pressures are usually found in the adsorption column, while atmospheric or lower pressures are required in the regeneration step for PSA and VSA mode, respectively [14].

- **Temperature Swing Adsorption (TSA)**

  Similarly to the previous processes, TSA has the same principle, but in this case the adsorption-desorption process is driven by temperature differences [27]. It is increased from moderate temperature in the adsorption process to around 120 °C in the desorption step. This process is often employed to remove CO_2 (and water) in air separation units present at very low concentration [14], [18].

  Both TSA and PSA were employed in industry for the first time during the 1960s and the first materials used were mainly silica gel, activated alumina, metal oxides and zeolites. Nowadays, the types of materials have been changing and MOFs activated carbon and graphite more often employed in these processes [14]. Despite their efficacy in removing trace compounds, these processes also present longer regeneration times and high energy consumption, which have to be considered [14].

- **Electrothermal Swing Adsorption (ESA)**

  The working principle of ESA consists of passing electricity through a packed column. For that matter, the adsorbent material used has to have the ability to conduct electricity to encourage such type of swing. Due to these characteristics, ESA presents lower costs, when compared to TSA and PSA [14].

1.3 Thesis Outlook

This thesis focuses on MOFs for CO_2 capture in two different aspects: (i) the investigation of chemical and structural properties of MOFs for CO_2 capture, and (ii) the investigation and selection of industrially favorable MOFs by considering process requirements. In Chapter 2, the first aspect is discussed by focusing on the MOF design and synthesis, as well as the understanding of the interactions between CO_2 and MOFs. We will present a fundamental study of pyrene-based MOFs, which aims at understanding the influence of different metals and topologies of MOFs including the same ligand (i.e. TBAPy - 4,4',4",4"'-(1,3,6,8-pyrenetetrayl)tetrabenzoic acid) on the CO_2 uptake. The second aspect focuses on the industrialization of MOFs, which is presented in Chapter 3. The main goal of this study is to transfer the knowledge that has been developed for MOFs at a laboratory scale to real case scenarios of CO_2 capture processes and designing and synthesizing MOFs which have computationally been found to be promising for wet fuel gas carbon capture, considering the process design parameters.

While research groups usually synthesize a new MOF and only then, develop studies to assess

their performance in different fields and applications, in this thesis we aim at following two approaches: from "material to industry" as well as "industry to material".

The experimental results will be consolidated with computational results, which aim at giving a more powerful insight and understanding of the mechanisms occurring between the structures being studied and the adsorbates.

2 Investigation of Pyrene-based MOFs towards CO_2 Capture

2.1 Introduction

Pyrene is a four-benzene-ringed hydrocarbon discovered in 1837 [38] and has been used for several applications, including the synthetic dye industry due to its yellow colour, and as a fluorophore due to its outstanding emission properties [38]. The pyrene core allows for aromatic substitutions at different positions (Figure 2.1), making it a very suitable molecule as a substrate in the synthesis of compounds commonly used in organic electronics materials, such as light-emitter diodes (OLEDs) due to its emission properties, and solar cells and organic photovoltaics (OPVs) due to its absorption properties [38], [39].

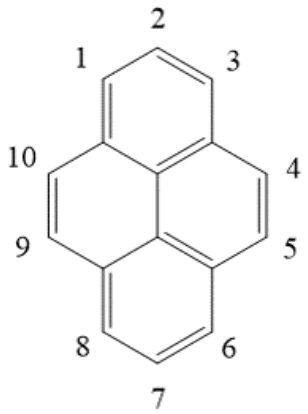

Figure 2.1 – Representation of the different positions for the aromatic substitutions in the pyrene core [38].

The organic molecule pyrene has been widely employed as ligand to contract MOF frameworks, mainly due to its optical and structural characteristics. Usually, the resulting MOF will reflect pyrene's properties, making it suitable for a given application. Moreover, the insertion of functional groups in the pyrene ligand can give rise to different aromaticities of the linker itself, as well as different MOFs structures with potential advantageous characteristics. Pyrene MOFs possess high surface area, convenient channels sizes and shapes as well as $\pi - \pi$ stacking

interactions, which can encourage the adsorption and separation of certain molecules [38]. For that matter, pyrene-based MOFs have already been investigated for CO_2 capture and are reported in the literature.

Because MOFs-based studies often only report the synthesis and applications of those particular structures, in this chapter, we aim at understanding the influence of different factors on the CO_2 uptake of pyrene-based MOFs. This study has been motivated by the literature [17], [38] and the factors whose effect wants to be assessed are: 1) metal, and 2) topology. Both studies work with a 1,3,6,8-tetrasubstituted pyrene, considering that these are the most electron-rich and active centers for an electrophilic substitution. The investigated ligand was thus 1,3,6,8-tetrakis(p-benzoic acid)pyrene (TBAPy) (Figure 2.4, meaning that benzoate groups were substituted at 1-,3-,6- and 8-positions. TBAPy, has the characteristic of having a rigid pyrene core, while the substituted groups at the edges, have rotational freedom. This ligand has been widely studied due to its ability in making MOFs fluorescent while responding to small guest molecules [38].

Each class of material designed for this study will be specified hereafter.

Group 1: M-TBAPy MOFs

Recently, Boyd et al. performed a study in which they generated and screened a database of 325'000 hypothetical MOFs for the CO_2/N_2 selectivity as well as the CO_2 uptake [17]. From the results, they were able to identify three main classes of CO_2 binding sites: A1) parallel aromatic rings; A2) metal-oxygen-metal bridges; and A3) open metal sites (OMS). When they compared the results of all these three classes for their affinity for H_2O, the class of the parallel aromatic rings (A1) was found to be promising for CO_2 binding and presented lower Henry coefficients for H_2O (i.e. less affinity for H_2O) than the other two classes A2 and A3 [17]. From their experimental results, they observed that a pyrene-based MOF (i.e. with parallel aromatic rings) allows for a near-optimum interaction with CO_2, while this structure lacks of hydrogen-bonding sites for its interaction with H_2O. Its higher affinity for CO_2 compared to H_2O makes this material very suitable for wet flue gas carbon capture. Moreover, by varying the metal ion in the MOF structure, it is possible to tune the distance between the aromatic rings to allow for higher interaction with the molecule of interest. The predictions show that the ideal distance should be 6.5 - 7.0 Å (Figure 2.2) [17].

The optimal spacing of 6.65 Å is obtained when using Al(III) as metal the and near-optimum inter-aromatic spacings can be obtained with Ga(III). A larger distance ranging from 7.3 - 7.7 Å can be obtained using In(III) and Sc(III) (Table 2.1), which lead to less intense energy interactions with CO_2, and thus lower adsorption capacity [17].

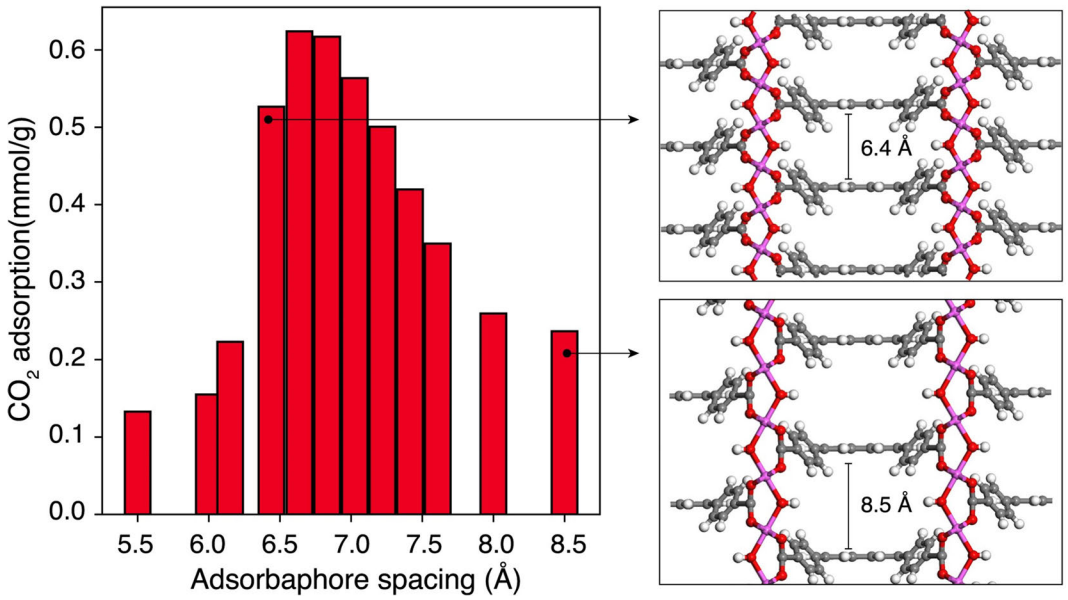

Figure 2.2 – Left, plot of the CO_2 adsorption as a function of the pyrene stacks distance at 0.15 bar and 313 K in hypothetical MOFs. Right, representation of the spacing between the aromatic rings of the pyrene ligand for an hypothetical MOF created with an Al cluster and pyrene ligand (metal node number 8 and organic linker number 67 (m8o67) adapted from [17]).

Table 2.1 – Spacing between aromatic rings in the MOFs structure as a function of the metal ion [17].

Metal Species	**Inter-aromatic Spacings [Å]**
Al(III)	6.65
Ga(III)	6.77
In(III)	7.27
Sc(III)	7.34

Group 2: Zn-TBAPy MOFs

Similarly, Kinik et al. report that some pyrene-based MOFs which possess the same ligand and metal in the synthesis can lead to different topologies. A particular attention was given to Zn-TBAPy MOFs which were found in the literature: Zn-(Ade)(TBAPy) 1 [40], Zn-(6BA)(TBAPy) 2 [41] and Zn-TBAPy 3 [42] and were investigated further in detail. These were selected based on the complexity of the reaction synthesis. The structural variety of these MOFs relies on the use of additional ligands (i.e. adenine (Ade), 6-benzylaminopurine (6BA), but also in many others parameters, such as the type of solvents used, the pH of the solution in which the reaction is performed, the molar ratio of the reactants, the presence of counter ions, among others [43].

In the present study, we aim at assessing the influence of different factors, such as metal and topology, on the CO_2 uptake capacity of pyrene-based MOFs. For that purpose, two classes were designed with the following characteristics:

- **Group 1: M-TBAPy MOFs**

  These MOFs have the same topology. They were chosen in order to have the same ligand (i.e. TBAPy) but different metals in the nodes (i.e. Sc-, Al-, In- and Ga-TBAPy);

- **Group 2: Zn-TBAPy MOFs**

  MOFs with different topology but same metal (i.e. Zn) and ligand (i.e. TBAPy).

In Figure 2.3, a scheme illustrating both sub-groups is shown.

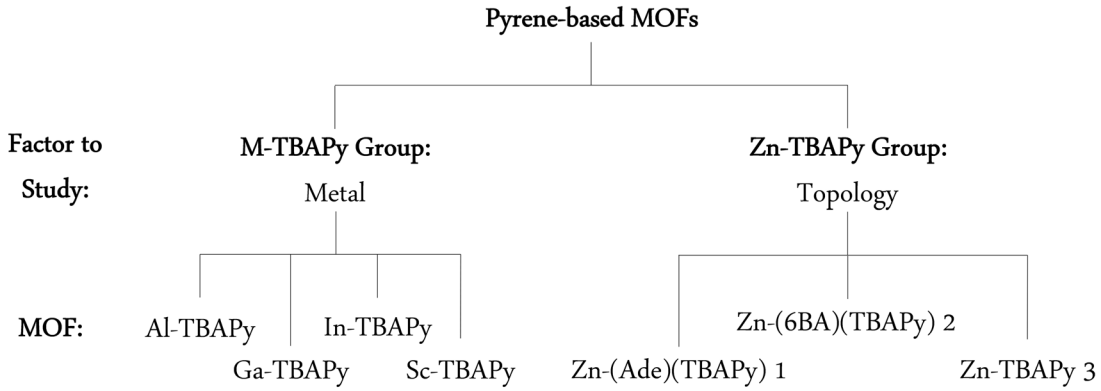

Figure 2.3 – Scheme of the pyrene-based MOFs project illustrating the factors to study and the respective samples for each sub-group.

2.2 Materials Synthesis

2.2.1 Pyrene Ligand

The ligand used for this study is 4,4',4",4"'-(1,3,6,8-pyrenetetrayl)tetrabenzoic acid and its synthesis reaction is described in Figure 2.4.

All chemicals were purchased from the commercial suppliers and used without further purification: dioxane (Sigma-Aldrich), 1,3,6,8-tetrabromopyrene (Sigma-Aldrich), (4-(ethoxycarbonyl)phenyl)boronic acid (Combi-Blocks), potassium phosphate tribasic (Sigma-Aldrich), tetrakis(triphenylphosphine)palladium(0) (Strem Chemicals), THF (Fisher Chemical) and HCl (Sigma Aldrich). The synthesis procedure was adapted from the literature [44], for the first step, and [45] for the second part.

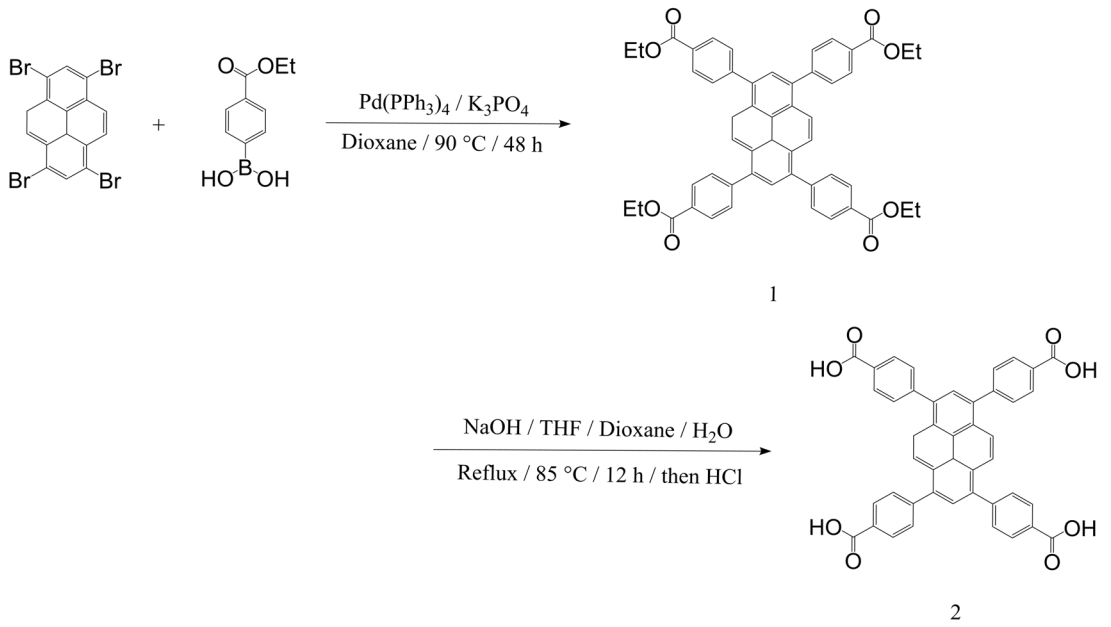

Figure 2.4 – The two-step synthesis reaction between 1,3,6,8-tetrabromo-3a1,5-dihydropyrene and (4-(ethoxycarbonyl)phenyl)boronic acid can be performed for the formation of H_4TBAPy (2).

For the synthesis of 1, 270 mL of dioxane were inserted into a 500 mL three-necked round-bottom flask, which was placed on a heating mantle and attached to a water condenser. Dioxane was constantly under stirring and it was degassed for 1.5 hours with argon using a high-efficiency sparger. While still purging the solvent with argon, 5 g of tetrabromopyrene, 8.25 g of 4-ethoxycarbonylphenyl boronic acid, 16.5 g of potassium phosphate tribasic and 0.75 g of tetrakis(triphenylphopsphine)-palladium(0) were added into the flask. The mixture was purged with argon for an additional 5 minutes. The reaction mixture was then heated up to 90 °C for 48 to 72 hours. Once the reaction was completed, 200 mL of water were added to the mixture, which was then led to cool down. Once at room temperature, the reaction mixture was filtered with a 200 mL glass Büchner funnel with a medium frit. The yellow solid on the frit was collected and washed with 100 mL of water twice as well as 200 mL of acetone. Then, to dissolve the desired product on top of the filter, 6 x 50 mL of boiling chloroform were used and flowed through the glass frit. The volume of the collected chloroform solution containing the desired product was reduced to 150 mL by blowing nitrogen through it at room temperature. 300 mL of methanol were then added into the solution and a yellow solid precipitate was formed. After 30 minutes, the precipitate was collected with a 200 mL glass Büchner funnel with a filter and the product was dried in a vacuum oven at 70 °C for 12 h (yield ≈ 55 % based on boronic acid).

For the synthesis of 2 (H_4TBAPy), 20 mL of concentrated NaOH were added to 1 g of 1 in a solution of THF/Dioxane/H_2O (ratio of 5/2/2). The mixture was then stirred under reflux at 85 °C overnight. H_2O was added to the mixture in order to dissolve the precipitate and the

solution was then stirred at room temperature for 90 minutes. The pH was then adjusted to 2 with concentrated HCl and the resulting yellow precipitate was recovered by filtration and washed with H_2O and diethyl ether and dried under vacuum. DMF (100 mL) was heated up until its boiling point and the product was added in order to dissolve it completely. The solution was left under stirring and filtered before it cooled down. Once it has reached room temperature, 300 mL of dichloromethane were added to the solution to precipitate H_4TBAPy only. Finally, the product was filtered under vacuum and dried overnight (yield ≈ 78 %).

2.2.2 Group 1: M-TBAPy MOFs

- $[Al_2(OH)_2(TBAPy)]\cdot(Guests)_x$ - [Al-TBAPy]

  All chemicals were purchased from the commercial suppliers and used without further purification: $Al(NO_3)_3\cdot 9H_2O$ (Alfa Aesar), dimethylformamide (DMF) (Roth), dioxane (Sigma Aldrich), HCl (Sigma Aldrich) and acetone (Sigma Aldrich).The synthesis was adapted from [17].
  A mixture of $Al(NO_3)_3\cdot 9H_2O$ (12 mg, 0.03 mmol) and H_4TBAPy (10 mg, 0.015 mmol) was introduced in a solvent mixture of DMF/dioxane/H_2O (4 mL, ratio 2/1/1). 10 μL of concentrated HCl were added into the mixture and the hydrothermal reaction was then performed in a ventilated oven at 85 °C for 12 hours. The heating and cooling rate were of 0.1 and 0.2 °C/min, respectively. Once the mixture had reached room temperature, the solid was recovered by filtration and washed with DMF in order to remove any non-reacted ligand.

- $[Ga_2(OH)_2(TBAPy)]\cdot(Guests)_x$ - [Ga-TBAPy]

  All chemicals were purchased from the commercial suppliers and used without further purification: $Ga(NO_3)_3\cdot xH_2O$ (Sigma-Aldrich), dimethylformamide (DMF) (Roth), dioxane (Sigma-Aldrich), HCl (Sigma-Aldrich) and acetone (Sigma-Aldrich).
  A mixture of $Ga(NO_3)_3\cdot xH_2O$ (7.67 mg, 0.03 mmol) and H_4TBAPy (10 mg, 0.015 mmol) was introduced in a solvent mixture of DMF/dioxane/H_2O (4 mL, ratio 2/1/1). 10 μL of concentrated HCl were added to the mixture and the hydrothermal reaction was then performed in a ventilated oven at 120 °C for 48 hours. The heating and cooling rate were of 0.1 and 0.2 °C/min, respectively. Once the mixture had reached room temperature, the solid was recovered by filtration and washed with DMF in order to remove any non-reacted ligand.

- $[In_2(OH)_2(TBAPy)]\cdot(Guests)_x$ - [In-TBAPy]

  $In(NO_3)_3\cdot 9H_2O$ was purchased from Alfa Aesar. The synthesis procedure was adapted from [45].
  $In(NO_3)_3\cdot 9H_2O$ (12 mg, 0.03 mmol) and TBAPy (10 mg, 0.015 mmol) were dissolved in a solution of DMF/dioxane/H_2O (4 mL, ratio 2/1/1) and 10 μL of concentrated HCl. The mixture was heated at 85 °C for 12 hours with a heating rate of 0.1 °C/min and a cooling rate was of 0.2 °C/min. The MOF was then washed three times with DMF. Yield ≈ 56%

based on $In(NO_3)_3 \cdot 9H_2O$.

- $[Sc_2(OH)_2(TBAPy)] \cdot (Guests)_x$ - [Sc-TBAPy]

  $Sc(NO_3)_3 \cdot xH_2O$ was purchased from Sigma Aldrich.
  $Sc(NO_3)_3 \cdot xH_2O$ (6.9 mg, 0.03 mmol) and TBAPy (10 mg, 0.015 mmol) were dissolved into a solution of DMF/dioxane/H_2O (ratio 2/1/1) and 10 μL of concentrated HCl. The mixture was heated at 85 °C for 12 hours with a heating rate of 0.1 °C/min and a cooling rate was of 0.2 °C/min. The MOF was then washed three times with DMF.

2.2.3 Group 2: Zn-TBAPy MOFs

- $[Zn_{1.5}O_{0.25}(Ade)(TBAPy)_{0.5}](NH_2Me_2)_{0.5} \cdot (Guests)_x$ - [Zn-(Ade)(TBAPy) 1]

  $Zn(NO_3)_2 \cdot 6H_2O$ was purchased from Sigma-Aldrich and used without further purification. The procedure was adapted from [40].
  A mixture of $Zn(NO_3)_2 \cdot 6H_2O$ (17 mg, 0.057 mmol), TBAPy (10 mg, 0.0146 mmol) and Ade (8 mg, 0.059 mmol) was dissolved into an acidic solution of DMF/H_2O/HNO_3 (5.5 mL/ 0.5 mL/4 drops). The mixture was then placed in the oven for 72 hours at 120 °C with a temperature heating and cooling rates of 0.1 and 0.2 °C/min, respectively. Yield ≈ 28% based on $Zn(NO_3)_2 \cdot 6H_2O$.

- $(Me_2NH_2)_2[(Zn_8(TBAPy)_3(6-BA)_4(\mu_4-O)(H_2O)_4] \cdot (Guests)_x$ - [Zn-(6BA)(TBAPy) 2]

  $Zn(NO_3)_2 \cdot 6H_2O$ and 6-benzylaminopurine (6-BA) were purchased from Sigma-Aldrich and used without further purification. The procedure was adapted from [41].
  A mixture of $Zn(NO_3)_2 \cdot 6H_2O$ (29 mg, 0.1 mmol), TBAPy (12 mg, 0.02 mmol) and 6-BA (5 mg, 0.02 mmol) was dissolved into a 4.5 mL solution of DMF/H_2O (4 mL/ 0.5 mL). The pH was then adjusted to 3 with concentrated HNO_3 (60 μL). The suspension was placed in the oven for 72 hours at 120 °C with a temperature heating and cooling rates of 0.1 and 0.2 °C/min, respectively. Yield ≈ 60% based on TBAPy.

- $[Zn_2(TBAPy)(H_2O)_2] \cdot (Guests)_x$ - [Zn-TBAPy 3]

  The procedure was adapted from [42].
  A mixture of $Zn(NO_3)_2 \cdot 6H_2O$ (9 mg, 0.030 mmol) and TBAPy (10 mg, 0.015 mmol) was dissolved in a mixture of DMF/dioxane/H_2O (5 mL, ratio 2/1/1), with 10 μL of concentrated HCl. The suspension was then heated to 120 °C for 72 hours with a temperature heating and cooling rates of 0.1 and 0.2 °C/min, respectively. The precipitate was then washed with DMF three times. Yield ≈ 41% based on $Zn(NO_3)_2 \cdot 6H_2O$.

2.3 Characterization

2.3.1 Powder X-Ray Diffraction (PXRD)

Powder X-ray diffraction measurements (PXRD) aim at confirming the physe purity of the crystalline structures. The data was collected with a Bruker D8 Advance diffractometer at ambient temperature using monochromated Cu Kα radiation (λ = 1.5418 Å), with a 2θ step of 0.02°. The predicted patterns were calculated from the respective crystal structures (Mercury 3.0). The background was subtracted for all the PXRD plots presented in this work.

In-situ capillary and variable temperature measurements (VTPXRD) were performed in order to further understand the thermal stability of the as-made In- and Sc-TBAPy MOF samples. The powders were loaded into a 1.0 mm quartz-capillaries and mounted on a standard Huber goniometer head and the corresponding PXRD patterns were recorded as a function of temperature (Figures 2.7). Such measurements were performed with a Bruker D8 Advance diffractometer by using a temperature controlled furnace up to 600 °C.

2.3.2 Thermal Gravimetric Analysis (TGA)

The thermal stability of the materials was assessed by TGA (PerkinElmer Thermogravimetry Analyzer). All measurements were performed under air flow, at atmospheric pressure, from 25 to 700 °C.

2.3.3 Elemental Analysis (EA)

Elemental analysis measurements have been performed for Ga- and Sc-TBAPy samples in order to assess the molecular formula of such structures, as they have not been reported yet. The data was obtained using a Thermo EA1112 Flash CHNS-O Analyzer. The measurement was performed in triplicate and approximately 8 mg of each MOF were used.

2.3.4 Adsorption Experiments

2.3.4.1 Brunauer-Emmett-Teller (BET) Surface Area & Pore Volume

The N_2 isotherms for the determination of the surface are and pore volume were performed with a BELSORP Mini (BEL Japan, Inc.), at 77 K, with N_2 as the probe. The range 0.06 - 0.25 p/p_0 of the N_2 adsorption isotherm was fitted accordingly to the BET equation in order to determine the overall surface area of the samples.

All samples were activated under dynamic vacuum (10^{-6} mbar) for 12 hours at the following temperatures: M-TBAPy group: 170 °C and 110 °C for the second group: Zn-TBAPy.

BET surface area and pore volume were the object of focus of computational chemists who

analyzed it via mathematical decomposition of the structure.

2.3.4.2 CO_2 & N_2 Adsorption Isotherms

The CO_2 & N_2 adsorption isotherms were mesured from 5 to 1200 mbar at 25 °C (Micromeritics 3Flex adsorption Analyser).

Experimental results were compared to isotherms computed with the grand canonical Monte Carlo (GCMC), thanks to the help of computational chemists.

2.3.5 Scanning-Electron Microscope (SEM)

To assess the morphology of the MOFs' crystals, the samples were glued onto aluminum pins with a carbon tape and coated with 7 nm thick iridium layer and observed with a FEI Teneo SEM instrument.

2.4 Results & Discussion

2.4.1 Group 1: M-TBAPy MOFs

In Group 1, pyrene-based MOFs with different metals were studied in order to assess the influence of the metal on the CO_2 uptake of such materials, depending on the distances between pyrene stackings of each structure. Four different metals have been investigated (i.e. Al, Ga, In and Sc) and the corresponding MOFs are structural analogues with each other, whose crystal structure is shown in Figure 2.5.

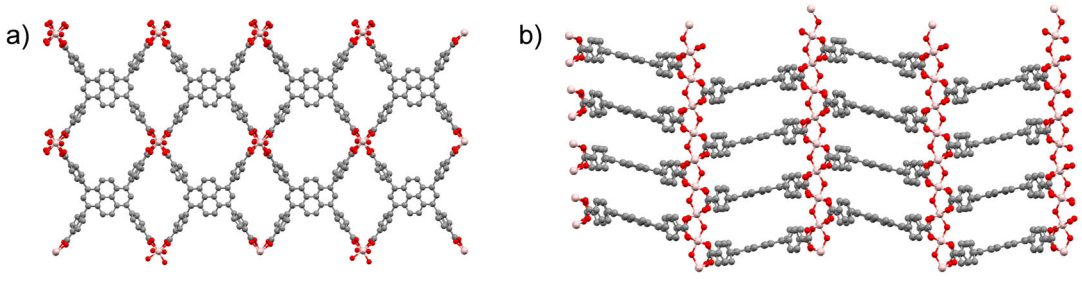

Figure 2.5 – Crystal structure representation of the M-TBAPy MOFs (where M = Al, Ga, In, Sc) in the: a) b axis with a rotation of z-90, and b) c axis. Colour code: M: pink; O: red; C: grey; H: white.

The metal sites of these structures form an infinite chain of $MO_4(OH)_2$ units (with M = Al, Ga, In, Sc) (Figure 2.5 b)) and each metal is bound to four TBAPy ligands (Figure 2.5 a)) [45].

While Al-TBAPy and In-TBAPy were synthesized according to a reported procedures [17],

[45], Ga-TBAPy and Sc-TBAPy are novel structures synthesized in Prof. Smit's group, whose synthesis conditions have not been published yet.

Bulk Characterization & Thermal Stability. To assess the crystal structures of all MOFs, PXRD measurements were performed (Figure 2.6). The experimental PXRD patterns of Al- and Sc-TBAPy are in good agreement with the predicted patterns for both as-made and activated samples. For In-TBAPy, an additional (broad) peak appears at approximately 9.5 - 10° (2θ) upon activation, while an additional peak between 9 - 10° (2θ) can be observed in both as-made and activated powder of Ga-TBAPy. In the following, the peak at 9 - 10° (2θ) will be referred to as "additional peak". In the original publication [45], it is reported that the additional peak in In-TBAPy results from a structural change (i.e. monoclinic distortion) upon desolvation, leading to a loss of crystallinity and symmetry. In contrast, an orthorombic unit cell was assumed for computations, wherefore the additional peak did not appear in the simulated structure.

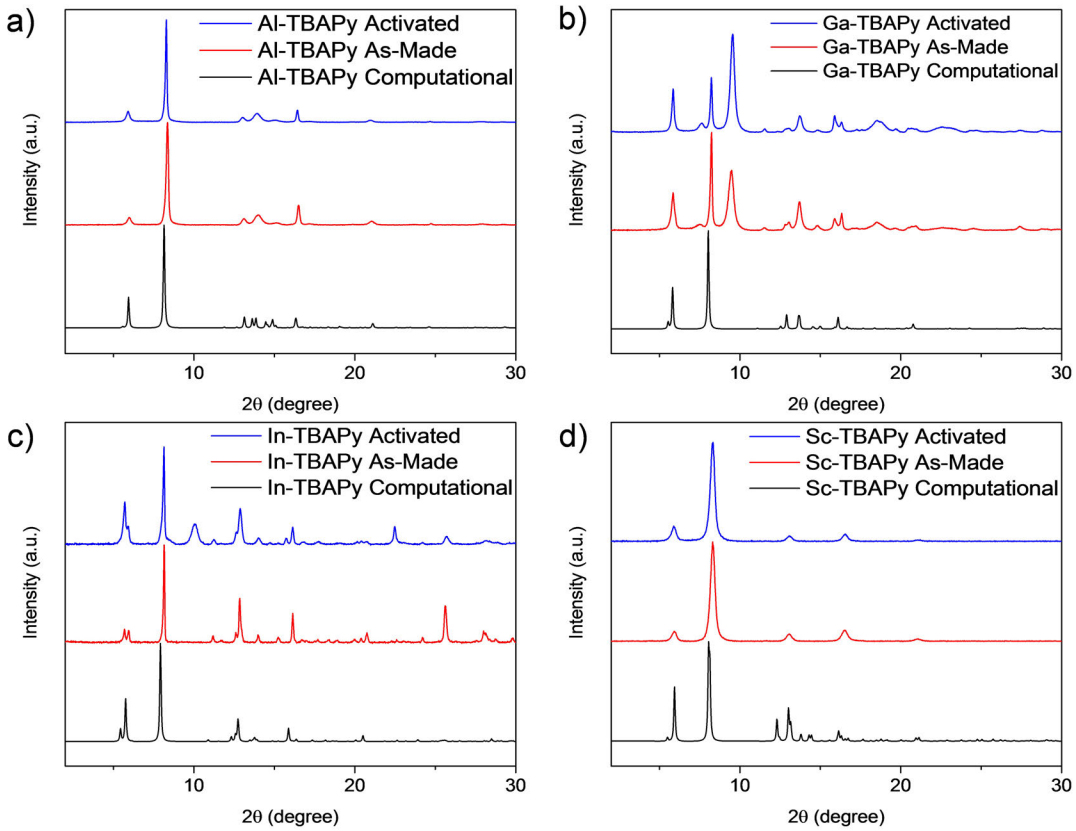

Figure 2.6 – PXRD of M-TBAPy MOFs: a) Al-TBAPy, b) Ga-TBAPy, c) In-TBAPy and d) Sc-TBAPy. Colour scheme: black, computationally derived predicted pattern; red, as-made; blue, activated.

Interestingly, the original (as-made) structure of In-TBAPy can be fully recovered by immersing the guest-free (activated) material in either DMF or a solvent mixture of DMF:Dioxane (v/v = 1/1) for at least 3 hours. The structure, however, cannot be restored if solvents, other than DMF, are used even if they were employed during the synthesis (e.g. H_2O, dioxane). This fact suggests that DMF plays indeed, an important role for the formation of the structure of In-TBAPy [45].

Concerning Ga-TBAPy, the additional peak is present for the as-made material, and the intensity increases upon desolvation. This phenomenon is currently not completely understood; however, it can be deduced that the additional peak appearance can be related to the presence or absence of the solvent molecules in the pores, resulting in the distortion of the structure, similar as it was observed in In-TBAPy.

To further understand the behaviour of Ga- and In-TBAPy, in-situ variable temperature PXRD measurements were performed, for which PXRD scans were taken at different temperatures, ranging from 25 to 600 °C. Concerning Ga-TBAPy results (Figure 2.7 a)), the in-situ variable temperature PXRD measurement led to a drastic decrease of intensity of the additional peak at 150 °C, until its full disappearance at 450 °C due to the collapse of the structure. Such phenomenom is not in agreement with what was observed in the PXRD measurement for the activated sample. It may be possible that the dynamic vacuum employed for the activation has an influence in the structure. For variable temperature PXRD measurement, vacuum is not applied, meaning that the energy applied might not be enough to remove the remaining solvent molecules from the structure. To understand the change in the intensity of the additional peak more clearly, Ga-TBAPy structure is still under investigation experimentally and computationally.

From In-TBAPy patterns (Figure 2.7 b)), the as-made material was heated up to 600 °C, but the additional signal (at 9.5 - 10° (2θ)) which is expected to appear upon desolvation, was not present at any of the scans taken at higher temperature. This result suggests that the removal of solvent molecules from the pores of the structure requires more energy to occur (i.e. by applying dynamic vacuum), as specified in the activation protocol. Another possible explanation would be that since the capillary is sealed to the machine to allow for its constant rotation during the measurement, it created a closed atmosphere and thus, a partial pressure which would not allow for the solvent evaporation.

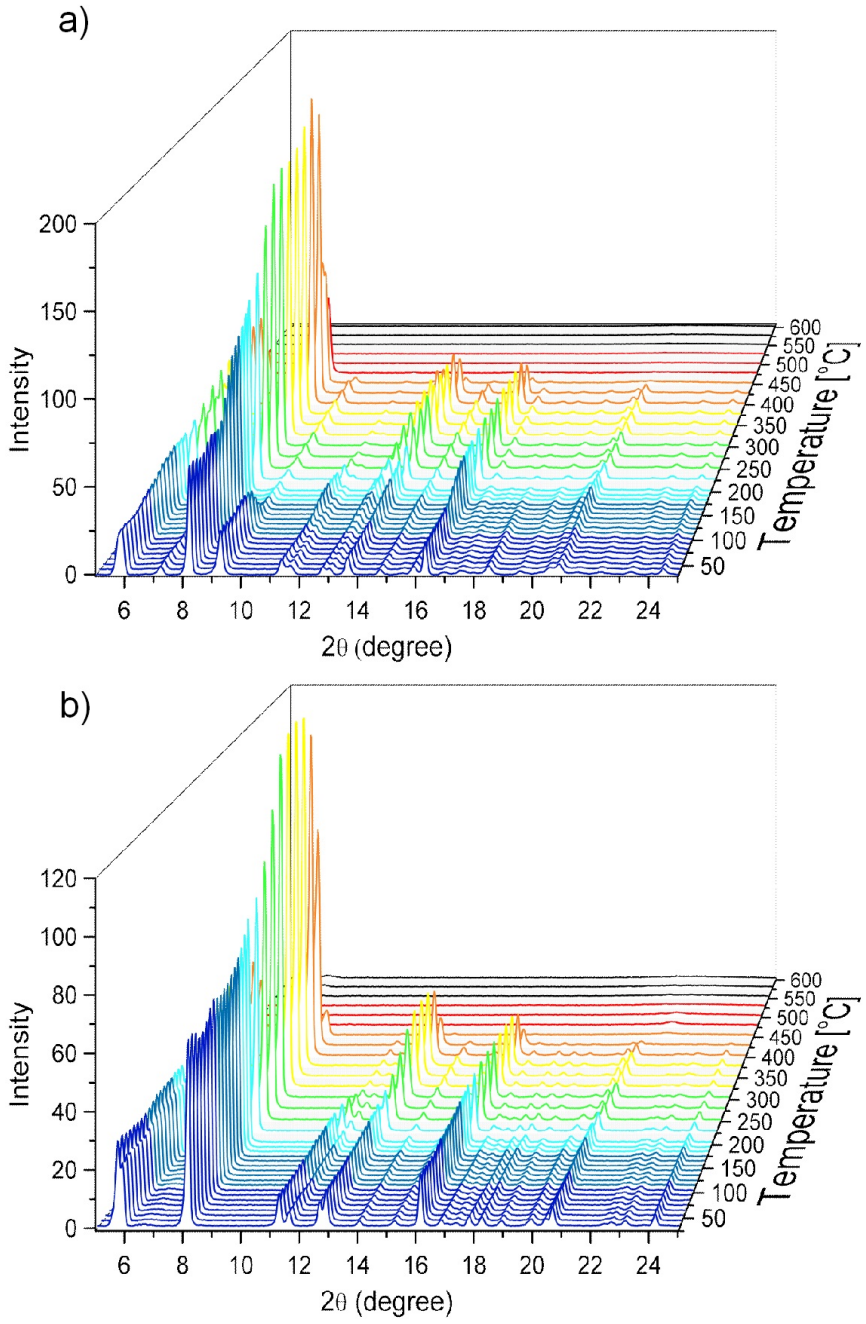

Figure 2.7 – In-situ variable temperature PXRD measurements of a) Ga-, and b) In-TBAPy.

The thermal stability of the MOFs was assessed through TGA (Figure 2.8 a)). All four structures present similar results: the solvent removal occurs until 200 °C, approximately, and they all start to decompose after 400 °C. The stability of Ga- and In-TBAPy was also confirmed with the variable temperature measurements, where we see a complete disappearance of all peak at 450 and 400 °C, respectively.

Considering that Ga- and Sc-TBAPy have not yet been published, elemental analysis (EA) on the activated powders was performed in order to determine the molecular formula of these MOFs, which were found indeed to be $Ga_2(OH)_2(C_{44}H_{26}O_8)$ and $Sc_2(OH)_2(C_{44}H_{26}O_8)$, respectively (Table A.1).

The N_2 isotherms for the determination of the surface area and pore volume of all structures were collected (Figure 2.8 b) and c)). The pore volumes of the materials were found to be: 0.835 cm^3/g (Al-TBAPy), 0.501 cm^3/g (Ga-TBAPy), 0.443 cm^3/g (In-TBAPy) and 0.466 cm^3/g (Sc-TBAPy) (Figure 2.8 c)). The vast majority of these MOFs (i.e. Ga-, In- and Sc-TBAPy) present a lower experimental pore volume than the computational one. In fact, there exist several computational methods for calculating the pore volumes of a microporous structures [46] and the one used for the calculations in this study corresponds to the probe-occupiable pore volume (PO). This method is based on a sphere of 1.63 Å radius (for N_2 as a probe) that is inserted in the network to obtain the accessible areas. However, the predicted data is not able to completely meet the results obtained from the experimental N_2 isotherms. This discrepancy can be due to assuming a perfect and completely desolvated crystal structure, while experimentally, there can be an incomplete solvent removal from the structure or a shrinkage of the pore after desolvation, which would lower the measured pore volume [46]. Moreover, for simulations, the structure is fully optimized and a perfect crystallinity and degree of symmetry are assumed during calculations, which would lead to higher pore volumes.

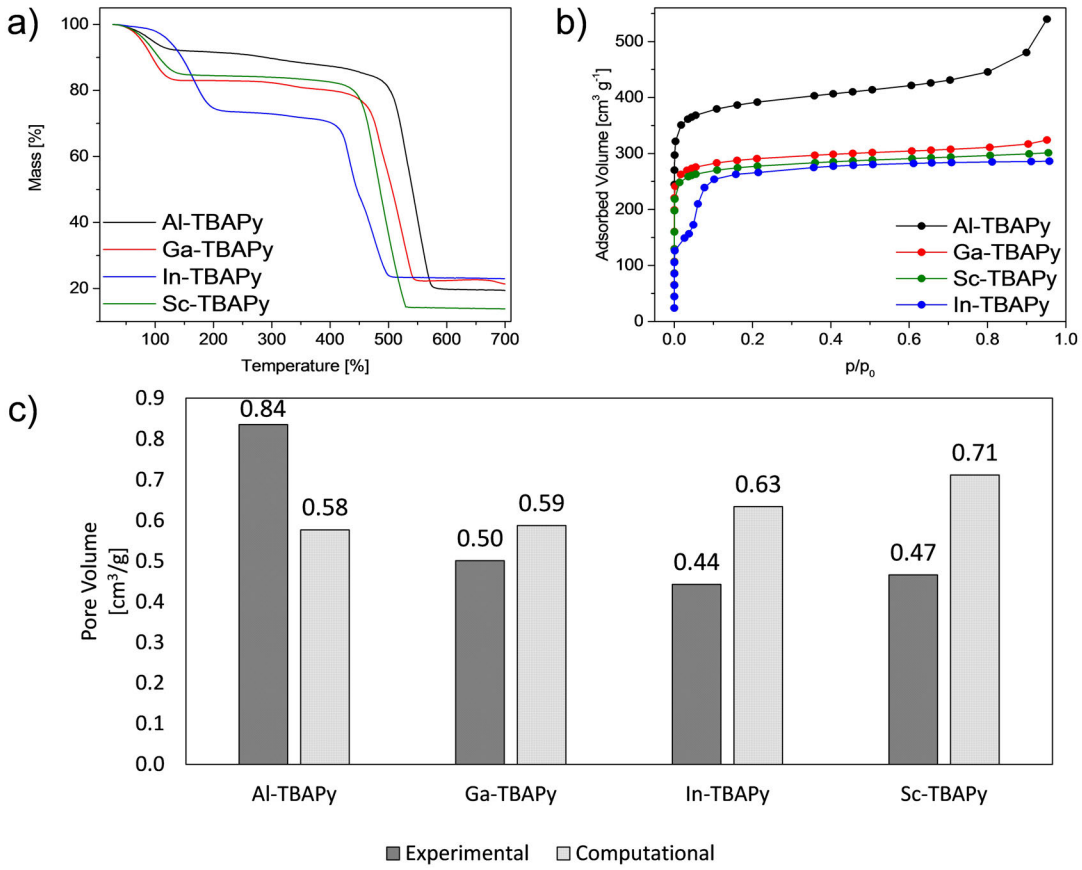

Figure 2.8 – a) TGA analysis, b) N_2 isotherms (collected at 77K), and c) pore volume measurements of M-TBAPy MOFs.

Even though the vast majority of the group shows a lower experimental pore volume than the predicted one, Al-TBAPy seems to be an exception, as calculations underestimate it by approximately 1.45 fold. From the Le Bail refinement (Figure 2.9), it is possible to notice that the Al-TBAPy experimental pattern (blue) shows a broadening of the peak at 13 °(2θ) compared to the perfectly crystalline computationally derived pattern (red).

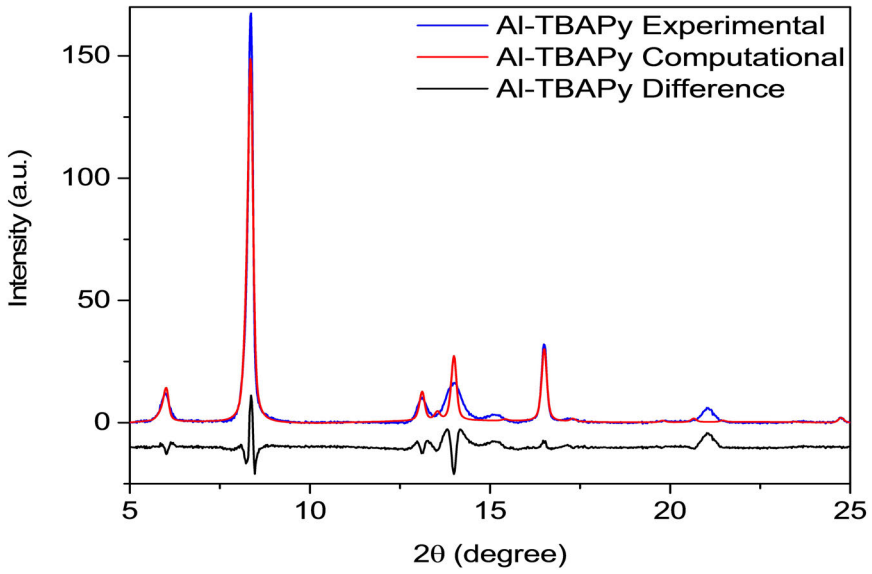

Figure 2.9 – Le Bail refinement for the as-made powder of Al-TBAPy.

Considering that lattice distortions (i.e. lattice parameters variation) can be described via the comparison of the experimental defected pattern with the ideal computational pattern [47], this broadening of the peak can be due to a micro-strain in the lattice, meaning that the lattice parameters of the experimental pattern do not correspond to the highly crystalline structure lattice parameters. These defects can also have an influence in the microporosity of the structure, which could explain such a high value compared to the predicted one.

Morphological Characteristics. SEM images were taken to assess the morphological characteristics of the four M-TBAPy MOFs (Figure 2.10). All crystals present distinct shapes: flake-like crystals for Al-TBAPy, squared sheets for Ga-TBAPy, while cubes and spheres for In- and Sc-TBAPy, respectively. Although the synthesis conditions were very similar for all MOFs, there are clear distinctions in the morphological features. All structures were obtained without any phase impurity, as it can be seen from the SEM images as well as the PXRD patterns.

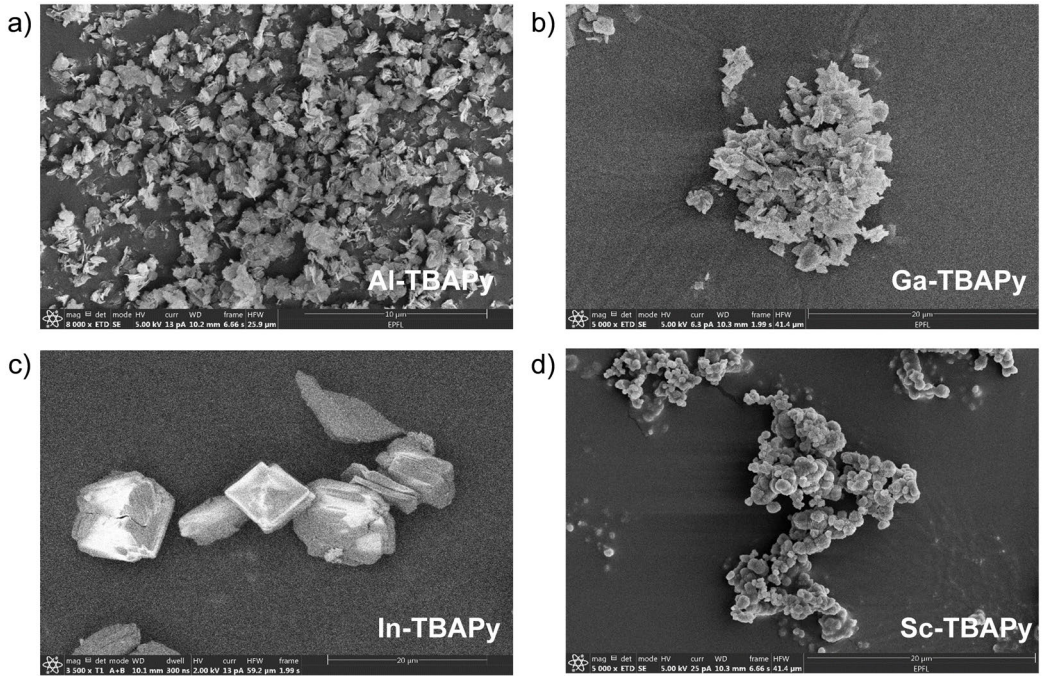

Figure 2.10 – SEM images of a) Al-, b) Ga-, c) In- and d) Sc-TBAPy displaying homogeneity, shape and size.

Sorption Study. Boyd et al. [17] reported that, since they possess near-optimum inter-aromatic spaces, M-TBAPy MOFs with Al(III) and Ga(III) metal centers should present a higher CO_2 uptake than those of In(III) and Sc(III). In fact, when the two latter metal centers are used in M-TBAPy MOF synthesis, they lead to structures presenting a higher distance between the pyrene stacks, which can range from 7.3 to 7.7 Å (Table 2.1). Considering that during adsorption, CO_2 interacts with the network in that exact same region, a higher distance leads to lower interaction energy.

All four structures were tested for CO_2 and N_2 uptake at 25 °C (Figures 2.11). Concerning CO_2 adsorption, as expected, Al-TBAPy behaves the best, showing the highest adsorption capacity at all pressures (from 5 to 1200 mbar). Ga- and Sc-TBAPy behave similarly, with Ga- having a slightly higher uptake at lower pressures. Finally, In-TBAPy results in the lowest uptake of all structures. However, if compared with the other MOFs at pressures lower than 200 mbar, In-TBAPy shows a very similar adsorption capacity. From the computational investigation and considering the relative variations between the pyrene stacks distances for all MOFs, Ga was expected to present a higher adsorption (closer to the one of Al-TBAPy) since the inter-aromatic distance in both structures differ of less than 0.12 Å from each other and are near the optimum value. However, if the additional peak (whose position is very similar to the one of In-TBAPy) corresponds to a distortion in the lattice (similarly to what occurs with In-TBAPy), a change in the pores shape and size may be possible, which would affect the CO_2 uptake of this material. This suggests that guest molecules might have a higher influence in

the crystalline structure of Ga-TBAPy than expected. Such impact needs further investigation but it might explain why the computational results differ from the experimental ones (Figure 2.11 a)).

As mentioned beforehand, In-TBAPy undergoes a structural change upon activation, it is possible that this phenomenon is also affecting its adsorption performance as for Ga-TBAPy. In fact, simulations assume a perfectly crystalline network with a high degree of symmetry, whereas experimentally this is often not the case. Such fact can explain why the experimental results In-TBAPy are much lower than the predictions.

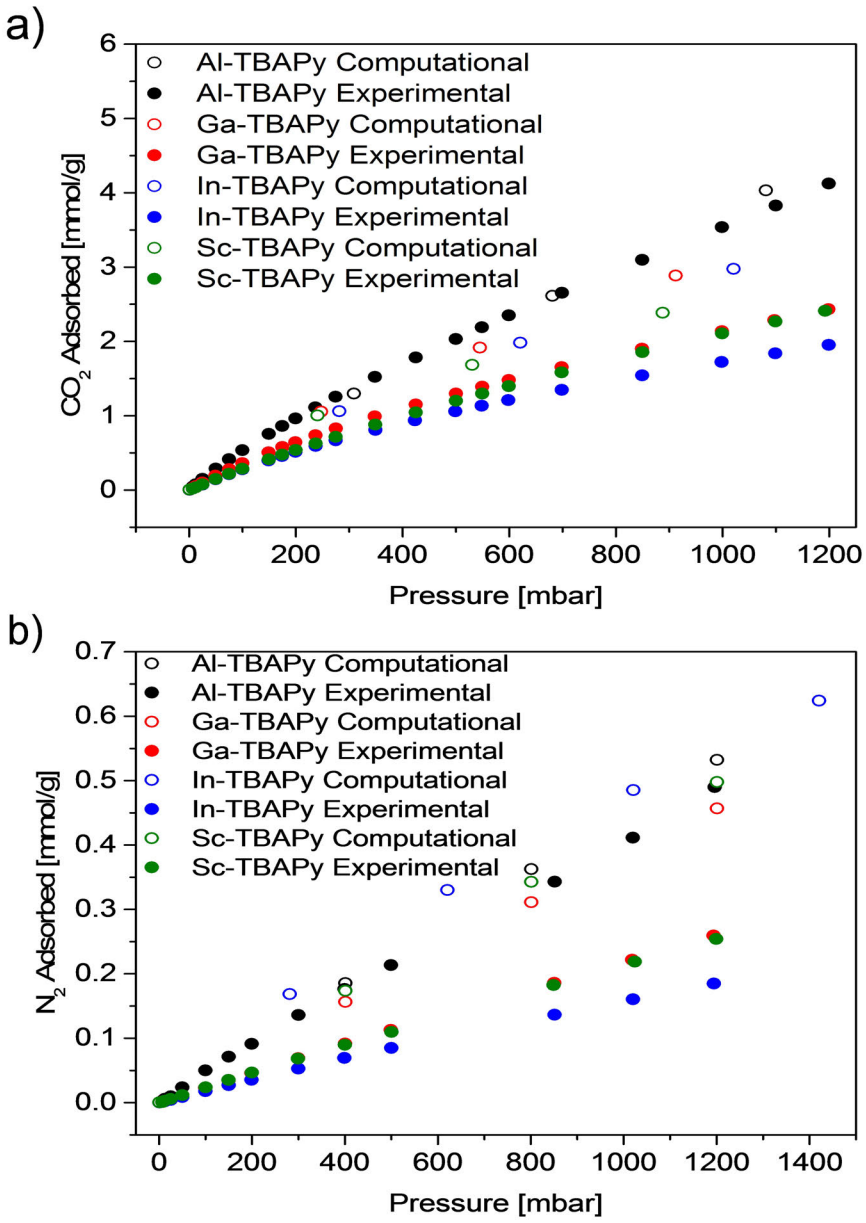

Figure 2.11 – CO_2 and N_2 experimental (filled) and computationally predicted (empy) adsorption isotherms of M-TBAPy MOFs.

Al-TBAPy is the structure that corresponds the best with the computationally predicted CO_2 isotherm, while all the other MOFs (Ga-, In- and Sc-TBAPy) show a slightly higher variations with the respective predictions. Such discrepancies might be due to the fact that the framework was kept rigid while performing the Monte Carlo simulations. Moreover, the inter-molecular interactions were modelled using the Lennard-Jones potential. For that matter, the dispersion energy parameters of the employed force field were scaled so that the interaction energy

between CO_2 and Al-TBAPy calculated with classical simulations agreed with first-principle calculations. For consistency in the study, these settings were employed for the calculation of all isotherms of all M-TBAPy MOFs and deviations of 2 % were expected for Al-TBAPy and 9 % for Sc-TBAPy, for instance. Moreover, the binding energies of CO_2 in the pyrene stacks for each of these MOFs were determined (Table A.2). These were performed by Density Functional Theory (DFT) and classical simulations based on an uniformal force field. Considering that all values calculated (based on DFT and FF) are in good agreement for all MOFs, except from Ga-TBAPy. This suggests that all isotherms (except the ones from Ga-TBAPy) have been predicted with a high degree of accuracy.

Considering that all MOFs presented in this group are structural analogues, the CO_2 binding site is located in between the pyrene stacks for all structures (Figure 2.12).

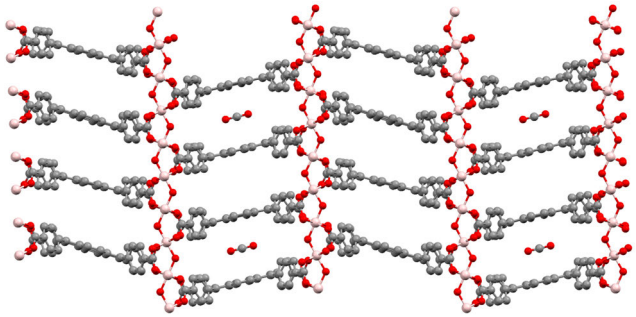

Figure 2.12 – Preferential binding site for CO_2 for the M-TBAPy MOFs (where M = Al, Ga, In, Sc) from c axis. Colour code: M: pink; O: red; C: grey; H: white.

In the correlation graphs (Figures 2.13 a) and b)), the CO_2 uptake [mmol/g] has been plotted as a function of the inter-aromatic spaces [Å] between pyrene stacks at: a) 200 mbar and b) 1 bar. In both figures an increase of the inter-aromatic distance, leads to a lower CO_2 adsorption at both pressures. Interestingly, even though Sc-TBAPy presents the largest distance (i.e. 7.34 Å), its adsorption capacity is still higher than the one of In-TBAPy, which possesses an pyrene stack distance of 7.27 Å. These results suggest that both factors (i.e. pore volume and inter-aromatic distances) play an important role in the CO_2 uptake of these structures and that a compromise between them has to be found for an optimal performance. Such theory can be confirmed as the difference of CO_2 uptake between In- and Sc-TBAPy increases with increasing pressure (from Figure 2.13 a) to b)). This suggests that the interactions between the structure and the gas molecules adsorbed become less important at higher pressures.

Concerning the N_2 isotherms, the relative trend of all structures was analogous to what was observed for CO_2 adsorption but the overall uptake was 8 times lower. This phenomenon can be explained by the fact that N_2 is a non-polar molecule, meaning it can hardly interact with the MOF structure, contrary to CO_2, which presents a large quadrupole moment. Considering that the interaction parameters have been adjusted for the Al-TBAPy system in the case of CO_2 adsorption, the N_2 data is acceptable but further investigation is needed from the

computational side to tune the interaction parameters for the simulations.

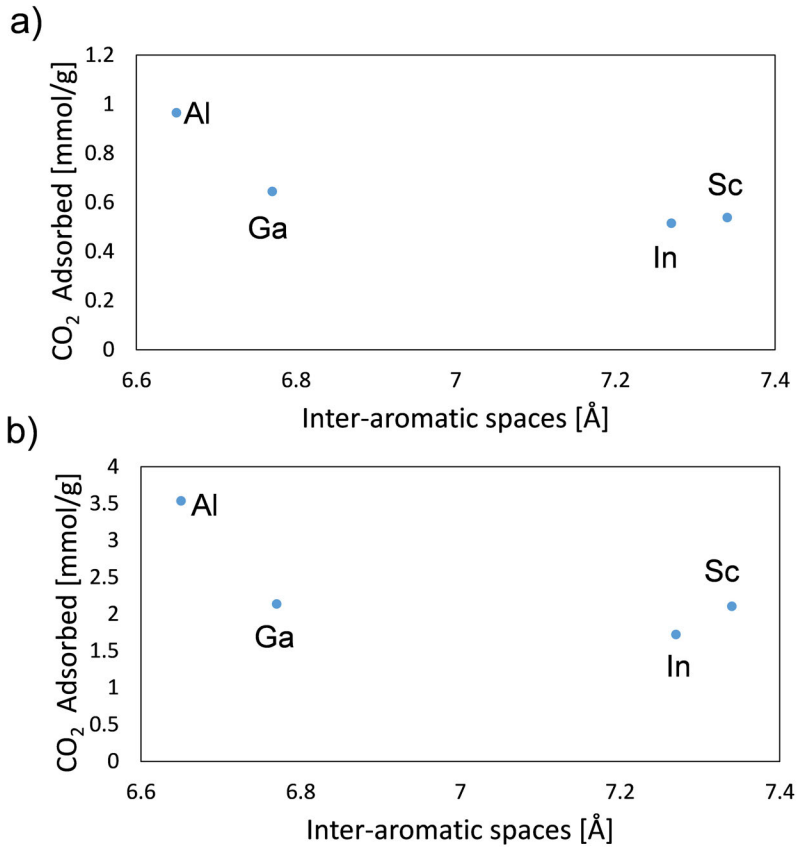

Figure 2.13 – Correlation plots for M-TBAPy samples at: a) 200 mbar and b) 1 bar.

In conclusion, the choice of the metal in MOF synthesis is of great importance as it can have an influence on the inter-aromatic distances, which consequently can affect the interactions between the adsorbent and adsorbate and thus, the CO_2 uptake. Overall, the results are in good agreement with the reported studies and simulations [17], [38], confirming a successful synthesis of all structures and adsorption measurements. The unexpected trends with In and Ga-TBAPy can be due to structural changes occurring upon activation of the sample. However, the computational predictions assume perfect crystal structures, making it more difficult to simulate extremely realistic case scenarios (which might sometimes present defects, structural changes, among other factors).

2.4.2 Group 2: Zn-TBAPy

In group 2, structures composed of a Zn(II) metal center and TBAPy as the ligand are studied. Even though the metal and ligand are the same for all structures, these MOFs present different topologies, either with the use of different modulators or solvents, or with the use of additional

ligands, such as adenine (Ade) or 6-benzylaminopurine (6-BA), as for: Zn-(Ade)(TBAPy) 1 and Zn-(6BA)(TBAPy) 2, respectively.

The crystal structure of Zn-(Ade)(TBAPy) 1 (Figure 2.14) presents an octahedral cage formed by four Ade ligands and six Zn(II) ions (two in the apical positions and four in the equatorial positions). The equatorial Zn(II), allow for bridging the cages, forming infinitely long columnar channels in the a direction. This structure allows this for the formation of two different types of pores: the acid-pore corresponding to where the carboxylate deprotonated oxygens atoms are pointing in (with a pore dimension of 7.9 x 4.9 Å), and a base-pore, with the Watson-Crick face of Adenine facing in (pore dimensions 5.4 x 6.9 Å) [40]. Both ligands are deprotonated in the structure which enunciates the need for counter-ions in order to balance the net charge of the network. Anderson et al. confirmed indeed the presence of cationic species near the carboxylate groups in the acid-pores: dymethyl ammonium chloride ($[NH_2Me_2]^+$) via X-ray photoelectron spectra (XPS) [40].

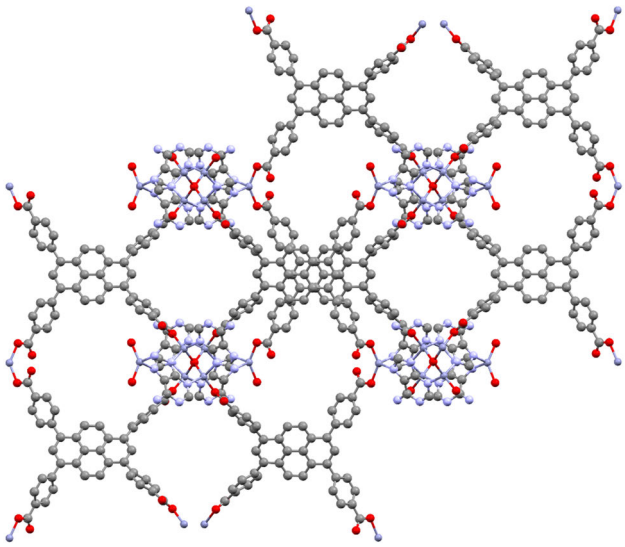

Figure 2.14 – Crystal structure of Zn-(Ade)(TBAPy) 1 along the c axis. Colour code: Zn: dark purple; N: light purple; O: red; C: grey.

Similarly to the first Zn-TBAPy structure, also Zn-(6BA)(TBAPy) 2 is an anionic MOF, as pyrene and 6BA are both deprotonated. For that matter, the same type of cation is present to counter-balance the charge: $[NH_2Me_2]^+$. Figure 2.15 a) elucidates the pyrene stacks, whereas Figure 2.15 b), shows the presence of two different types of pores along the c axis with opening dimensions of ca. 6.4 x 4.2 Å and 5.5 x 2.8 Å [41].

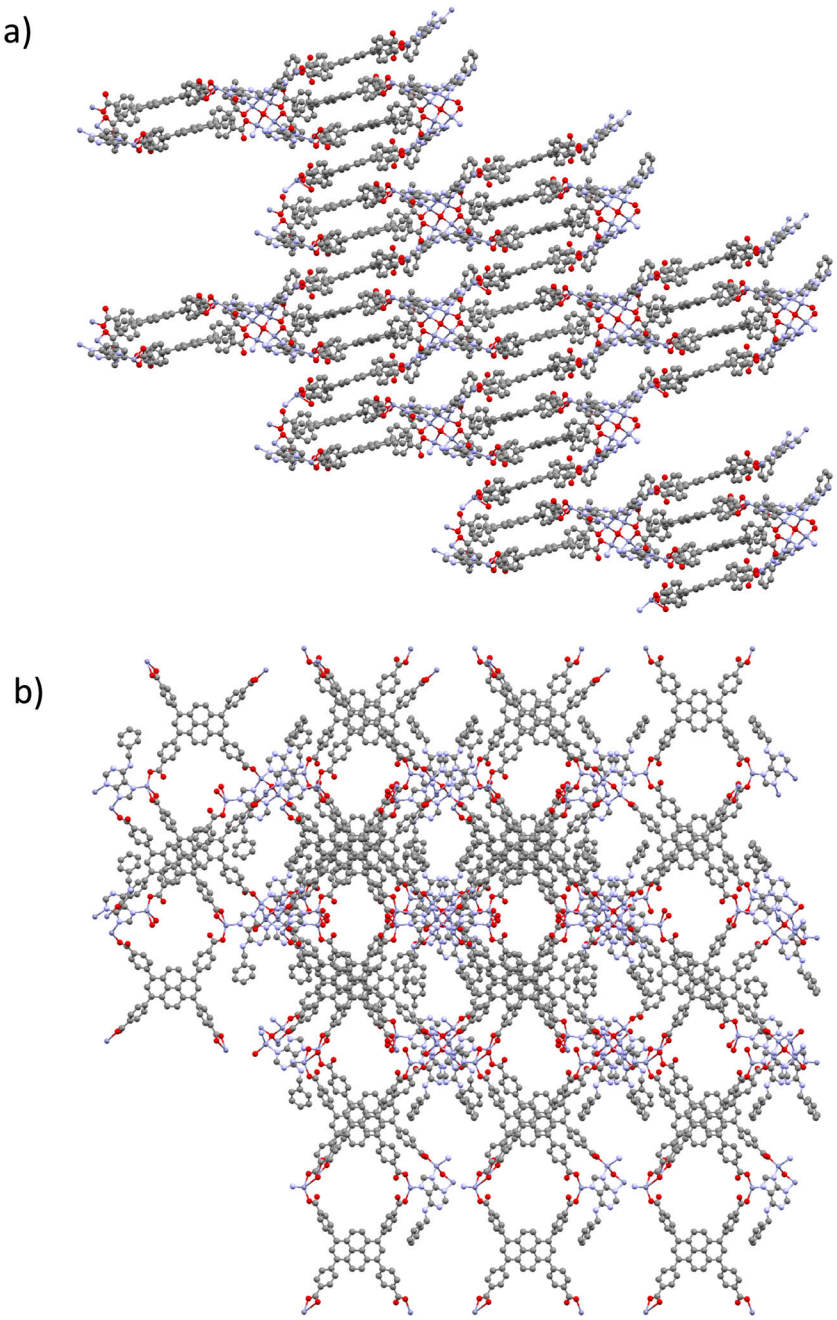

Figure 2.15 – Crystal structure of Zn-(6BA)(TBAPy) 2: a) b axis with a rotation z+90 and b) c axis. Colour code: Zn: dark purple; N: light purple; O: red; C: grey.

Zn-(TBAPy) 3 is a structure which undergoes a structural change upon desolvation as shown in Figure 2.16 a) along the a axis and b) the b axis. In Figure 2.16 b), it can be observed that the 2D structure, formed of paddlewheel units, allows for the crosslinking of the adjacent layers upon activation (i.e. removal of the H_2O molecules coordinated) [42]. Stylianou et al.

demonstrated via molecular dynamics (MD) simulations that Zn undergoes a transformation from square-pyramidal (before activation) to tetrahedral (after activation) and that the ligand undergoes a geometrical local distortion as well as a rotation and displacement, which allows for the cross-linking of adjacent layers, going from a 2D to a 3D structure (Figure 2.16 b)) [42]. Similarly to In-TBAPy, this transformation is reversible upon removal/addition of the H_2O molecules in the network. Such structure gives rise to two different types of pores with very similar maximum/minimum dimensions: 9.9 x 3.6 Å and 10.0 x 3.4 Å [42].

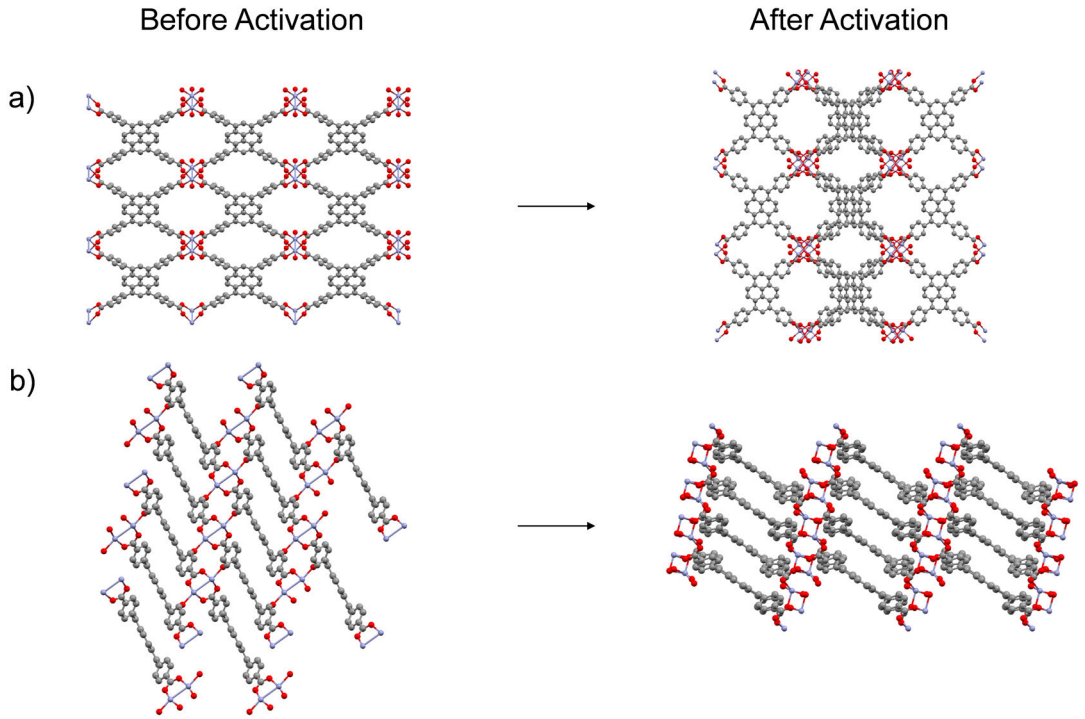

Figure 2.16 – Crystal structure of Zn-(TBAPy) 3 before and after desolvation: a) a axis and b) b axis. Colour code: Zn: dark purple; N: light purple; O: red; C: grey.

Bulk Characterization & Thermal Stability. To assess the crystal structure of these MOFs, PXRD measurements were performed (Figures 2.17 a) - c)). Concerning Zn-(Ade)(TBAPy) 1 and Zn-(6BA)(TBAPy) 2, the positions of the diffraction peaks at a short range order are in good agreement with the computational ones. At a longer range (for $2\theta > 10$), however, the peaks become broader and less defined. Such phenomenon suggests some loss of crystallinity of the powder but the structural backbone of these MOFs is still maintained. Interestingly, as it can be seen in Figure 2.17 c), Zn-TBAPy 3 undergoes a structural change upon activation. The PXRD pattern of the as-made material matches the computationally derived predicted pattern for the same MOF considering that the metal site is fully coordinated. On the other hand, after desolvation, the pattern of the activated sample is more in agreement with the computational pattern calculated from the open metal site structure. The peak at 10 °2θ is still present but its intensity is drastically reduced, meaning that upon activation, most (but

probably not all) of the H_2O molecules coordinated to the metal center were removed. The reduced intensities and broadening of the peaks at long-range order is an indication of a lower crystallinity of the MOF structure.

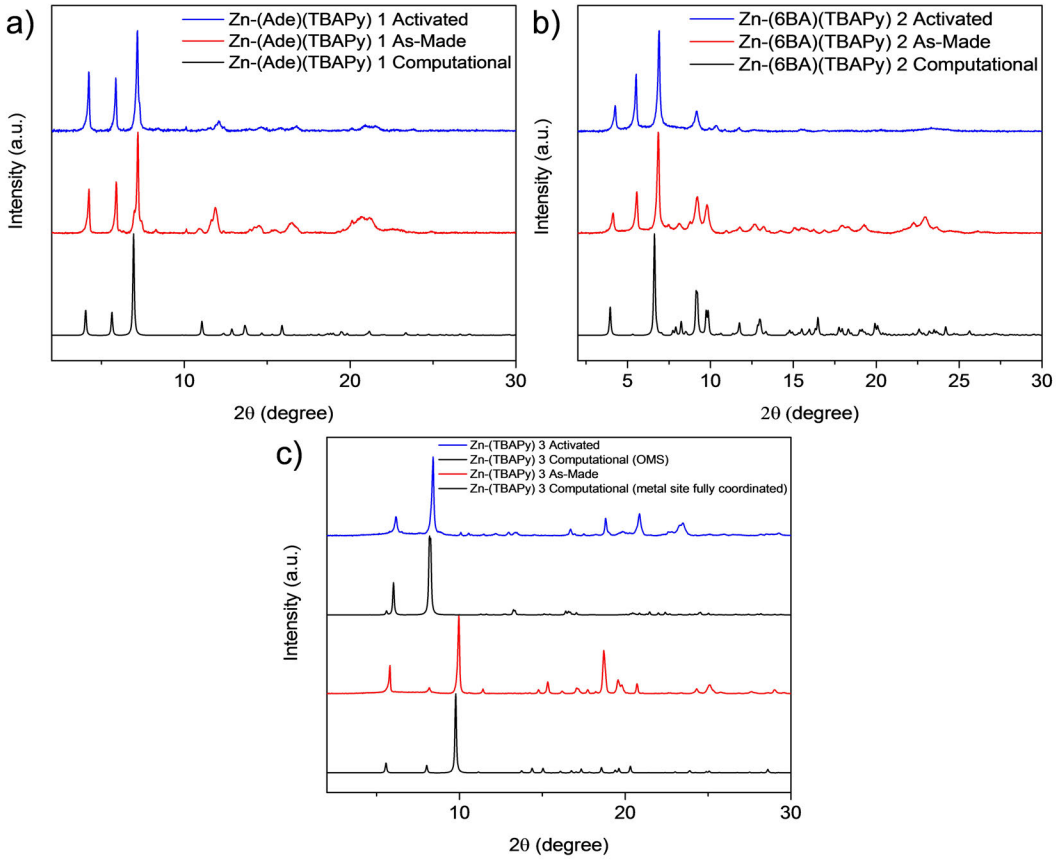

Figure 2.17 – PXRD of Zn-TBAPy: a) Zn-(Ade)(TBAPy) 1; b) Zn-(6BA)(TBAPy) 2 and Zn-(TBAPy) 3. Color scheme: black, computationally derived predicted pattern; red, as-made; blue, activated.

In-situ variable temperature PXRD measurements were collected on the as-made powders of all samples. Figure 2.18 a) and b) show that Zn-(Ade)(TBAPy) 1 and Zn-(6BA)(TBAPy) 2 structures are thermally stable up to 350 and 300 °C, respectively. Similarly, Zn-TBAPy 3 seems to maintain its structure up to 400 °C and the appearance of peaks at positions 6.5, 13.5 and 16.5 2θ (°) can be observed at temperatures higher than 100 °C, corresponding to the conformational change occurring upon the removal of H_2O and other guest molecules coordinated to the metal site.

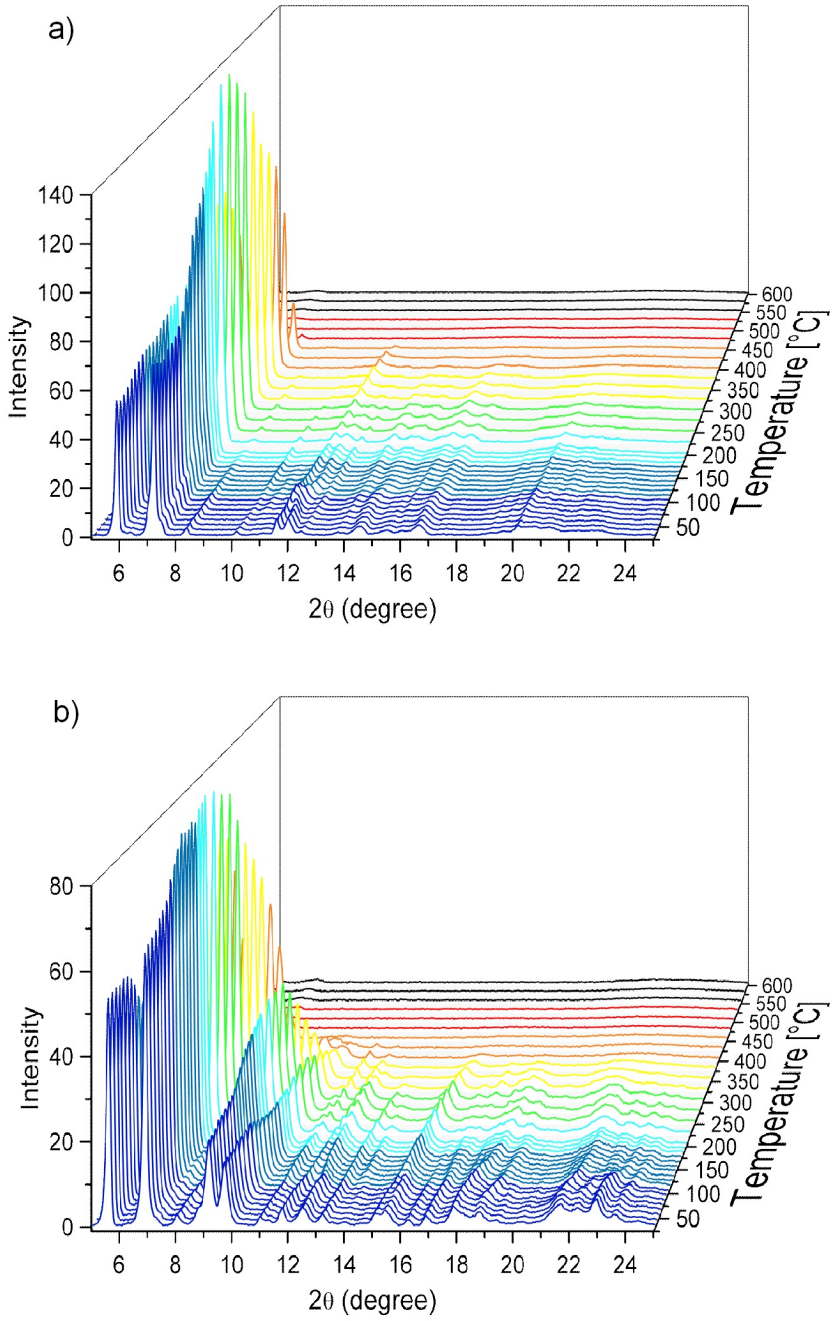

Figure 2.18 – Variable temperature PXRD patterns of a) Zn-(Ade)(TBAPy) 1 and b) Zn-(6BA)(TBAPy) 2.

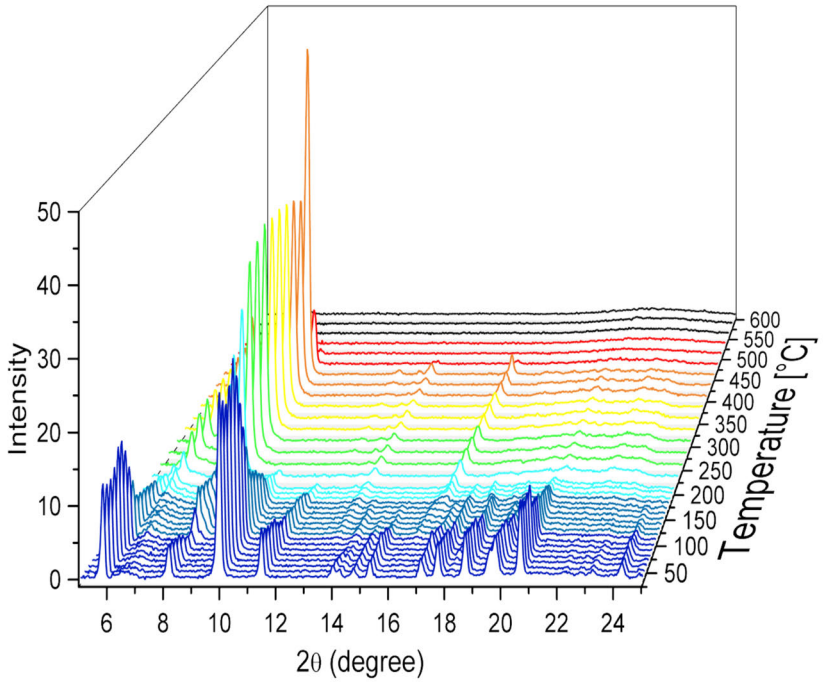

Figure 2.19 – Variable temperature PXRD patterns of and Zn-(TBAPy) 3.

The TGA profile for Zn-(Ade)(TBAPy) 1 (Figure 2.20 a)) shows a first decrease at approximately 100 °C, related to the removal of H_2O molecules, while the second decrease up to approximately 300 °C, corresponds to the loss of DMF and $Me_2NH_2^+$ [40]. At around 350 °C, the structure starts to decompose, as it was also confirmed by the variable temperature measurements (Figure 2.19 a)). Concerning Zn-(6-BA)(TBAPy) 2 (Figure 2.20 a)), the complete solvent removal occurs at 160 °C, while the coordinated H_2O molecules are being removed at 300 °C [41]. For Zn-TBAPy 3 (Figure 2.20 a)), it seems that the removal of guest and coordinated H_2O molecules occurs in a single step [42]. This structure is then stable up to 420 °C.

Type I adsorption N_2 isotherms at 77 K were measured for Zn-(Ade)(TBAPy) 1 and Zn-(TBAPy) 3 (Figure 2.20 b)) to determine the microporosity of these structures. Zn-(6BA)(TBAPy) 2 showed a type II adsorption isotherm in the same conditions. The pore volumes were found to be: 0.293, 0.045 and 0.275 cm^3/g for Zn-(Ade)(TBAPy) 1, Zn-(6BA)(TBAPy) 2 and Zn-(TBAPy) 3, respectively (Figure 2.20 c)), which are in good agreement with the computational ones.

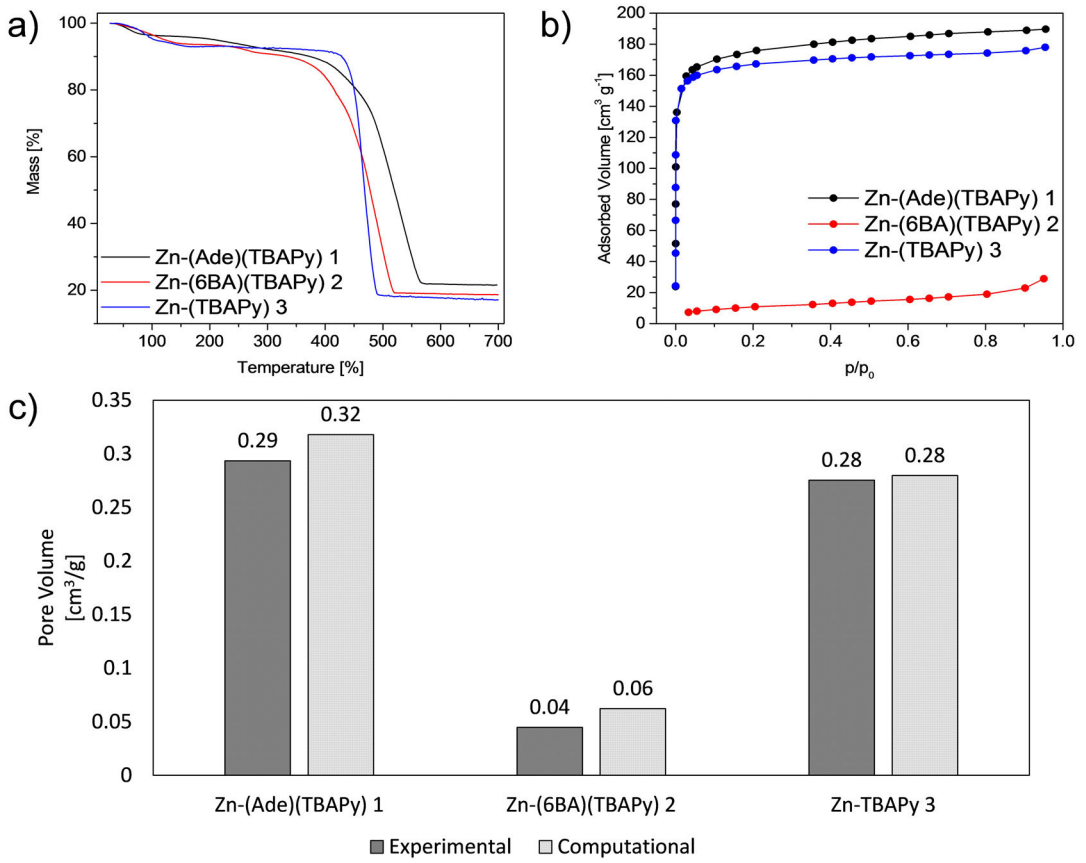

Figure 2.20 – a) TGA analysis, b) N_2 isotherms (collected at 77 K), c) pore volume measurements of Zn-(Ade)(TBAPy) 1, Zn-(6BA)(TBAPy) 2 and Zn-(TBAPy) 3.

Morphological Characteristics. SEM images of Zn-TBAPy MOFs show an overall homogeneity of the crystal shapes and sizes of all samples (Figure 2.21). Zn-(Ade)(TBAPy) 1 is composed of less defined crystals than Zn-(6BA)(TBAPy) 2 and Zn-(TBAPy) 3, which present a more spherical- and rod-like shapes, respectively. Although the structures are based on the same metal and ligand, the differences in synthesis conditions resulted in different crystal morphology.

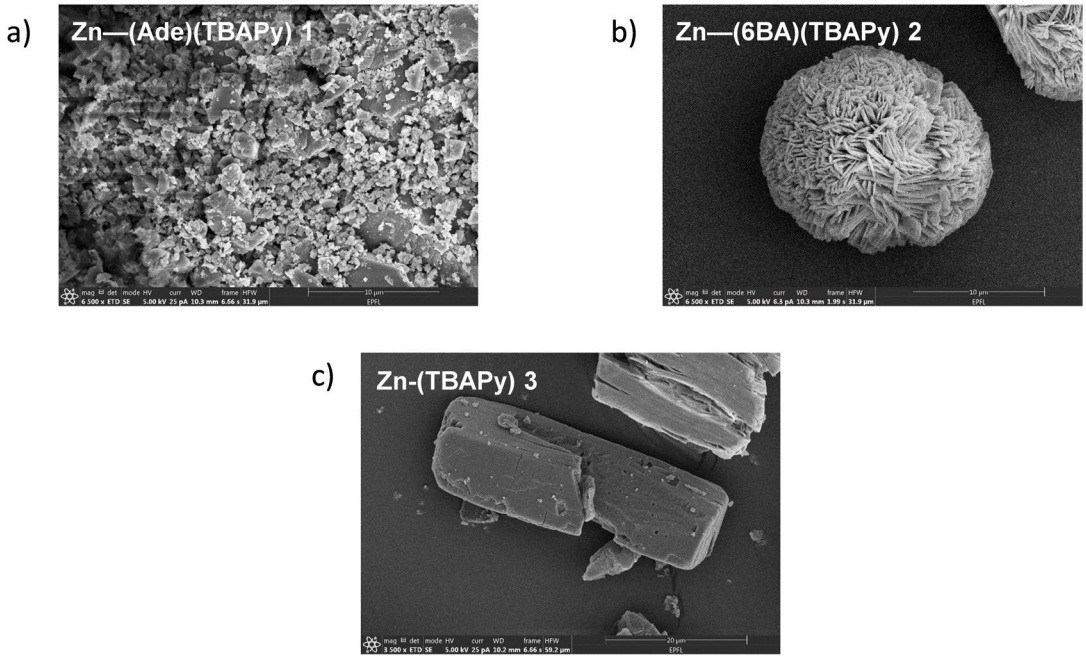

Figure 2.21 – SEM images of a) Zn-(Ade)(TBAPy) 1, b) Zn-(6BA)(TBAPy) 2 and c) Zn-(TBAPy) 3.

Sorption Study. The CO_2 adsorption isotherms at 298 K from 5 to 1200 mbar were measured and compared with the computationally derived predicted curves (Figure 2.22). For both N_2 and CO_2, the experimental results match well with the computational ones, apart from one structure: Zn-(Ade)(TBAPy) 1. To estimate whether the computational isotherms has been overestimated, the binding energies calculated using DFT and FF should be compared. If the value obtained with force fields differs too much from the DFT, then this might suggest that the calculated isotherm is not accurate enough.

Zn-(6BA)(TBAPy) 2 and Zn-(TBAPy) 3 (Figure 2.22 a)) present two different trends at low and higher pressures. In both regimes, Zn-(Ade)(TBAPy) 1 always outperforms the other structures. Considering that it presents larger pore dimensions and that adenine possesses an amino group are factors which can enhance the uptake and interactions with CO_2. However, further investigation to assess the influence of this particular structure on the CO_2 adsorption capacity is needed. At low pressures (up to 450 mbar), Zn-(6BA)(TBAPy) 2 outperforms Zn-(TBAPy) 3, while at higher pressures the opposite occurs. In the literature [48], it has been reported that at lower CO_2 loadings, the preferential binding sites would depend more on the enhanced interactions between the MOF and the CO_2 generated in smaller pores, rather than the influence of the BET surface area/pore volume. The microporous 1D channels of Zn-(6BA)(TBAPy) 2 possess a cross-sectional area of 5.5 x 2.8 Å [41]. Therefore, much stronger interactions with CO_2 can be expected compared to that of Zn-(TBAPy) 3, whose pore dimensions are 5.8 x 5.3 Å[42]. Consequently, the higher CO_2 uptake of Zn-(6BA)(TBAPy) 2 than that of Zn-(TBAPy) 3 at lower pressures can be attributed to its smaller pores. At higher pressures (after 450 mbar), all the preferential active sites of Zn-(6BA)(TBAPy) 2 have been

filled and the influence of pore size and molecule-molecule interactions increases. The CO_2 uptake rate starts to decrease and the larger pore volume of Zn-(TBAPy) 3 makes the difference and allows for a continuous uptake, outperforming Zn-(6BA)(TBAPy) 2. These differences observed in the structures showed that, although the metals are the same in all structures, different topology-related characteristics of Zn-TBAPy MOFs evoked different CO_2 adsorption performances.

For the N_2 adsorption isotherms, Zn-TBAPy 3 has the highest N_2 uptake. Zn-(Ade)(TBAPy) 1 and Zn-(6BA)(TBAPy) 2 present a lower uptake with Zn-(6BA)(TBAPy) 2 slightly outperforming Zn-(Ade)(TBAPy) 1. Interestingly, Zn-(Ade)(TBAPy) 1, which highly performed in the CO_2, presents the lowest N_2 adsorption of all three MOFs compared in this study. This may be attributed to higher affinity to CO_2 than N_2 but 2-component mixture adsorption isotherms should be calculated to verify it.

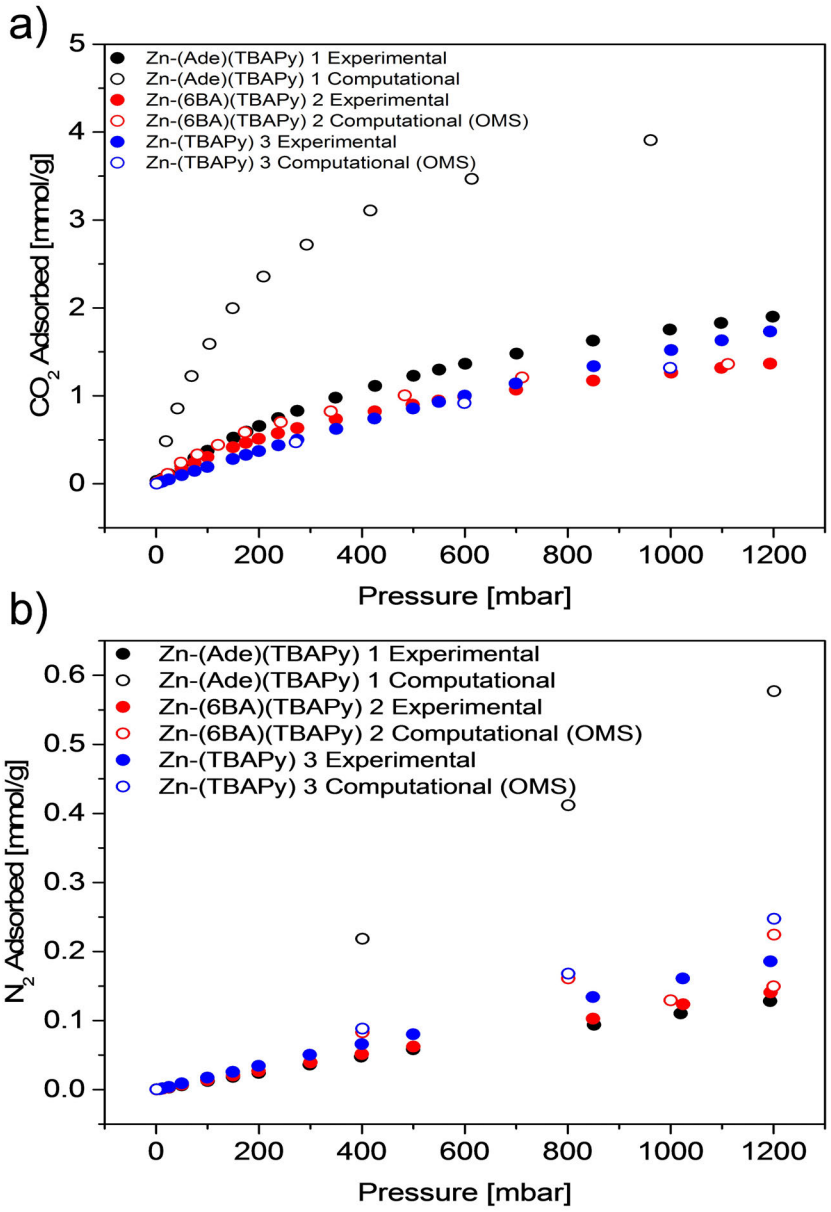

Figure 2.22 – CO_2 and N_2 experimental (filled) and computationally predicted (empty) adsorption isotherms of Zn-(Ade)(TBAPy) 1, Zn-(6BA)(TBAPy) 2 and Zn-(TBAPy) 3.

The CO_2 binding energies were computationally derived and the preferential binding sites for CO_2 in each Zn-(TBAPy) MOF structure are shown in Figure 2.23

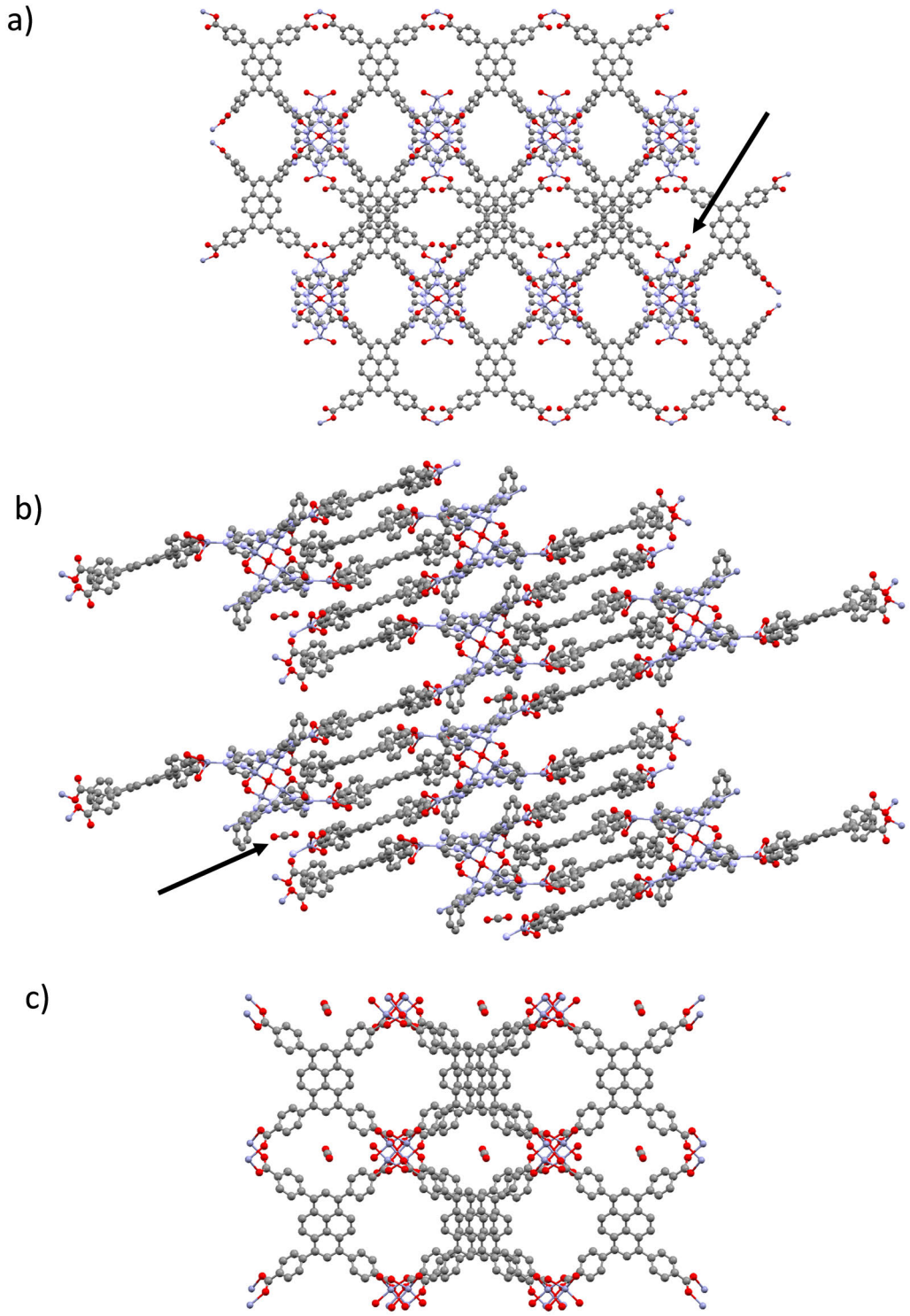

Figure 2.23 – Preferential binding sites for CO_2 in a) Zn-(Ade)(TBAPy) 1 (a axis), b) Zn-(6BA)(TBAPy) 2 (b axis, z+90) and c) Zn-(TBAPy) 3 (a axis). Colour code: Zn: pink; O: red; C: grey.

Figure 2.23 shows indeed that CO_2 binds to different adsorption sites in MOFs with the same metal and ligand but different topology. Contrary to the M-TBAPy study, where the CO_2 molecules would always be located in the pyrene stacks, in this case, this only occurred for Zn-(6BA)(TBAPy) 2 (Figure 2.23 b)). For Zn-(Ade)(TBAPy) 1 and Zn-(TBAPy) 3, CO_2 preferentially interacted with the structure in the pores (Figures 2.23 a) and c)).

In conclusion, the MOFs topology can play an important role in the CO_2 uptake. This molecule presents a quadrupole moment which can highly interact with the MOF network. The environment that these structures create can enhance MOF-CO_2 interactions, which is the parameter that seems to have the highest influence in adsorption at lower pressures. It was observed that ligands containing amino groups (i.e adenine) are able to enhance the CO_2 uptake. At lower pressures, it was found that smaller pores allow for stronger interactions and thus, facilitate the CO_2 uptake, while at higher pressures, this process was mainly affected by the pore volume.

3 Bridging the Academic Expertise with Industry for a Sustainable Future

3.1 Introduction

MOFs have been investigated as extremely promising candidates for efficient carbon capture by several research groups worldwide over the past three decades [49]. Publications usually report the synthesis, properties and applications of these structures at a laboratory scale. With a growing interest on CO_2 capture at large scales, investigating the industrial implementation of MOFs as adsorbants seems to be crucial. For that matter, the present chapter focuses on the implementation of these materials in industrial applications and thus, we attend to bridge the academic knowledge with the industry's requirements.

The Process-Informed design of tailor-made Sorbent Materials for energy efficient carbon capture (PrISMa) is a project which arised from the necessity of efficient sorbent materials for carbon capture. PrISMa is an international project with a wide range of partners, going from different universities worldwide to several companies which aim at designing cost-efficient carbon capture solutions for a wide range of different CO_2 sources, uses and destinations.

The PrISMa project has been designed with three main parts [50]:

- **Stage 1: Process Simulation**

  It consists at developing a platform through the identification of a family of CO_2 sources and sinks. A data-set of millions of materials were screened in the context of process design for CO_2 capture. For that purpose, thermodynamic and transport properties were calculated and a life-cycle analysis was performed. Such characteristics gave then rise to the requirements that drove the materials screening and testing in the following stages of the project [50].

- **Stage 2: Computational Screening**

  The previous data-set of candidate materials for CO_2 capture was screened for a given CO_2 source and sink. At this stage of the project, the capture technology was the object of

focus. The goal was to rank and thus select the most promising materials out of millions hypothetical and already known and synthesized MOFs in terms of their CO_2 adsorption capacity. The thermodynamics and transport properties of such materials, expressed via "key performance indicators", were assessed via computational calculations and the ones that showed a higher performance than the pre-selected reference material (i.e. Al-PMOF) would then pass onto the next stage [50].

- **Stage 3: Synthesis & Characterization**

  From the group of most promising structures for wet fuel gas carbon capture, the most feasible ones from the synthesis point of view were aimed to be synthesized and fully characterized. For the synthesis, hydrothermal treatments were used. The characterization consisted of PXRD analysis, BET surface area and pore volume measurements, TGA, volumetric measurements for CO_2 and N_2 isotherms, as well as SEM imaging, for the confirmation of the chemical and structural identity of the structures. This work was performed at EPFL Sion, and will be discussed further in detail in the present thesis.

3.2 Computational Screening

Prior the synthesis and characterization of materials for wet fuel gas applications, screenings were performed by computational chemists to identify the most promising structures. After defining all the process requirements for carbon capture, there was the need for a protocol which would be able to screen and assess the performance of millions of materials which would perform better than a certain benchmark. An automated workflow was developed based on a screening protocol (initially developed for COFs) and it was tuned in order to obtain a set of comparable geometries of experimental MOFs with accurate charges [51]. From a dataset of experimental MOFs (i.e. CoRE-MOFs-2019), a first screening was performed in order to remove the problematic structures (e.g. with overlapped atoms) and then, a geometry optimization through DFT calculations, leading to a total of 3'200 optimized MOFs, was done.

The benchmark material was chosen (i.e. Al-PMOF) and pure component CO_2 and N_2 adsorption isotherms were computed through a workflow developed by Prof. Smit's group. The computational data was then compared to the experimental results obtained in the laboratory, for the same materials, which confirmed that the predictions were accurate enough and that could be used on a larger scale.

The process models developed on Stage 1 of the project (i.e. process simulations), depend on a mixture adsorption (and not simply on single component isotherms). After interconnecting the pure component isotherms and the process models, a test screening of 450 structures was performed. Their performance was tested for PSA and TSA processes for a coal-fired power plant, whose CO_2 composition was 14%. The performances of the structures were then ranked and the 15 top performing structures which provided higher CO_2 purity and lower process energy demand than the benchmark (i.e. Al-PMOF) were selected and are listed in Table 3.1.

The names of the structures are provided as reported in the Cambridge Crystallographic Data Center (CCDC) (i.e. CCDC reference code).

3.3 Matrix Selection

Even though all structures listed in Table 3.1 are reported in the literature and their synthesis conditions are available, several parameters have to be taken into account if these structures had to be synthesized at a large scale, as this project aims to do.

Thus, aiming at a possible future industrial application, the yield of the reaction, the commercial availability of the ligand, and the prices of both metal and ligand were assessed (see Table 3.1), to determine which structures should firstly be synthesized. From that screening, the following 4 structures were selected as the first MOFs to be investigated: PEFJUF, HAKSIY, EKOPEA and DORFOG.

Table 3.1 – MOF structures computationally been found to be promising candidates for wet fuel gas carbon capture [I].

Structure	Yield [%]	Metal		Ligand			Ref.
		Element	Price [CHF]	Ligands	Commercial Availability	Price [CHF]	
ZIMHUA	50% based on Zn	Zn	108.- for 500g	H2bct bib	No	-	[52]
PEFJUF	Not reported	Al	128.- for 1kg	P2O5	Yes	80.- for 1kg	[53]
HAKSIY	53% based on metal	Fe Mg	112.- for 500g 114.- for 500g	H2bdc 1,2,4-triazole	Yes	47.- for 500 g of BDC 342.- for 500 g of triazole	[54]
WARJAC	44% based on Ni	Ni	120.- for 500 g	H3tzdc	No	-	[55]
GAYFUJ	86% based on ?	Cd	138.- for 500g	H2BPZ	No	-	[56]
IQUCOO	70% based on Mg	Mg	134.- for 500g	H4EBTC	Yes	284.- for 250 mg	[57]
IYESIQ	37% based on Cd	Cd	138.- for 500g	H2aze bib	No	-	[58]
EKOPEA	86% based on Cd	Cd Ca	138.- for 500g 57.80.- for 500g	m-H2BDC	Yes	23.30.- for 500 g	[59]
HEZPIL01	Not reported	V	-	Many	-	-	[60]
HIWKII	11%	Mn K	143.- for 500g -	pzdo	Yes	970.- for 1 g	[61]
WENKEH	55% based on H2ispc	Pr	551.- for 250g	H2ispc	No	-	[62]
DORFOG	Not reported	Mg	56.1.- for 500g	L-malic acid Na2CO3	Yes	38.2- for 5g	[63]
HILJUJ	36% based on Ce(III)	Ce	236.- for 500g	Pyridine-3,5-dicarboxylic acid (NH4)2SO4·2H2O	Yes	27.2.- for 1g	[64]
GAWJEV	64% based on Zn(II)	Zn	108.- for 500g	H4bptc	No	-	[65]
DAFSOV	83%based on Zn	Zn	108.- for 500g	Pyrazine bdc triazole	Yes	- 47.- for 500 of BDC 248.- for 5g of triazole	[66]

3.4 Materials Synthesis

3.4.1 $[Fe_3O(bdc)_3][Mg_2(trz)_3(H_2O)_4Cl_2]$ - HAKSIY

$FeCl_3 \cdot 6H_2O$ was purchased from Sigma-Aldrich and used without further purifica-tion. The procedure was adapted from [54].

$FeCl_3 \cdot 6H_2O$ (54.0 mg, 0.3 mmol), $Mg(OAc)_2 4H_2O$ (43.0 mg, 0.2 mmol), terephthalic acid (H2bdc, 51.2 mg, 0.4 mmol) and 1,2,4-triazole (23.0 mg, 0.4 mmol) were dissolved in a a23 mL Teflon-liner with 3.0 g of DMF and 850 mg trifluoroacetic acid (TFA). After stirring the mixture for 2 hours, the Teflon cup was sealed into a stainless steel autoclave. The autoclave reaction was performed in the oven at 150 °C for 24 hours. Yield ≈ 53% based on metal.

3.5 Characterization

3.5.1 Powder X-Ray Diffraction (PXRD)

The data was collected with the same specifications as described in the Chapter beforehand. The predicted patterns were determined from the respective crystal structures (Mercury 3.0).

3.5.2 Thermal Gravimetric Analysis (TGA)

The thermal stability of the material was assessed by TGA as mentioned in Chapter 2.3.

3.5.3 Adsorption Experiments

3.5.3.1 Brunauer-Emmett-Teller (BET) Surface Area & Pore Volume

The BET surface area and the pore volume measurements were performed with the same instrument and method specified in Chapter 2.3.

Before the measurement, the sample was desolvated under dynamic vacuum (10^{-6} mbar) with a slow, step-wise activation, as follows: 80 °C, 100 °C, 120 °C, 150 °C, for 10 hours eahc and 180 °C for 5 hours.

BET surface area and pore volume were also predicted computationally via molecular dynamics simulations.

3.5.3.2 CO_2 & N_2 Adsorption Isotherms

The CO_2 & N_2 adsorption isotherms were performed from 5 to 1200 mbar at 25 °C (Micromeritics 3flex Adsorption Analyser).

Such isotherms have also been predicted through Monte Carlo simulations for comparison with the experimental results.

3.5.4 Scanning-Electron Microscope (SEM)

To assess the morphology of the MOFs' crystals, the sample was glued onto aluminum pins with a carbon tape and coated with 7 nm thick iridium layer. The sample was observed with a FEI Teneo SEM instrument.

3.6 Results & Discussion

Among the 15 top performing structures listed in Table 3.1, four structures were selected for the synthesis in the laboratory: PEFJUF, HAKSIY, EKOPEA and DORFOG, as they presented a commercially available and low cost ligand as well as easier reaction conditions and higher yield, compared to the remaining ones (i.e. hydrothermal reactions up to 5 days). From all these attempts, HAKSIY (Figure 3.1) was successfully synthesized. In the original publication of PEFJUF [53], the reaction conditions were not reported in detail. Even though different conditions have been tried, the synthesis was not successful. EKOPEA was synthesized successfully; however, it was found to be highly unstable, which collapsed upon the removal of guest molecules from the pores (either via activation or through solvent exchange). The synthesis of DORFOG was not reproducible as in the case of PEFJUF.

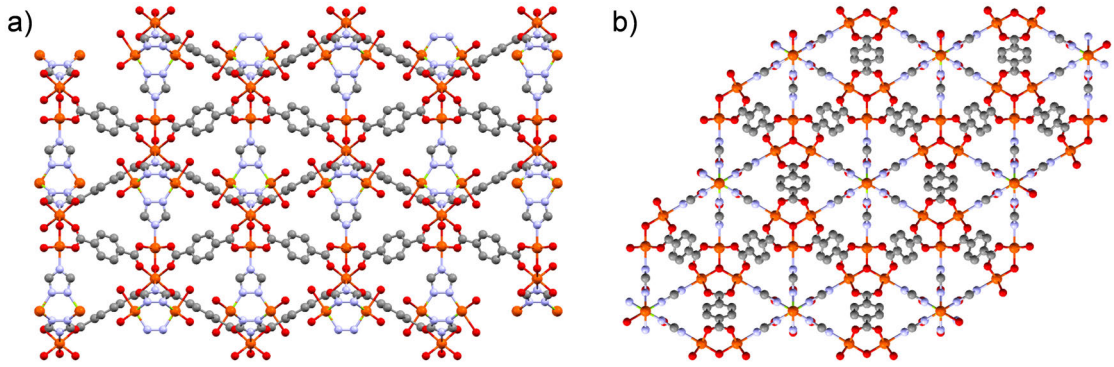

Figure 3.1 – SEM images of HAKSIY, with the corresponding view from the a) b axis and b) c axis.

Bulk Characterization & Thermal Stability. The PXRD pattern of HAKSIY was collected at ambient conditions for both: as-made and activated samples (Figure 3.2). The peak positions of both patterns are in good agreement with the computationally derived predicted pattern, meaning that the structure was obtained without any phase impurity. At a long range order, it

is possible to observe some loss of crystallinity degree upon activation due to the broadening of the main peaks at 9.2 ° (2θ) and the decrease in intensity of the peaks at higher order.

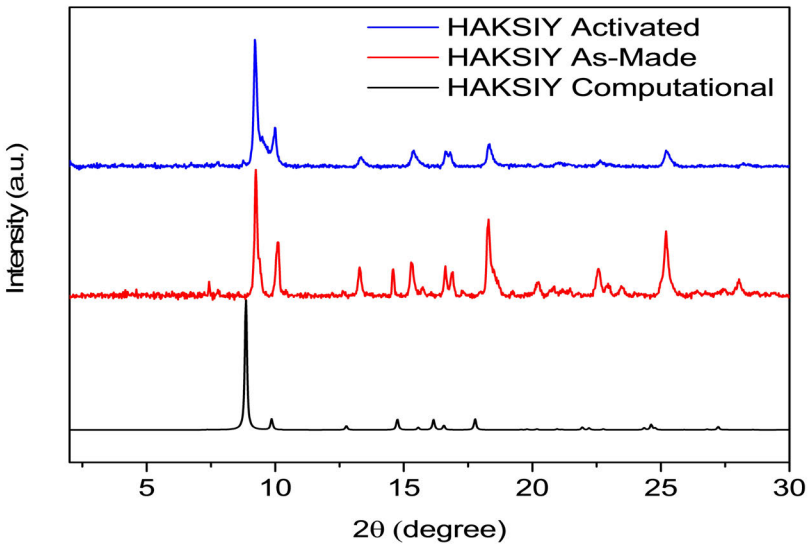

Figure 3.2 – PXRD patterns of the as-made and activated HAKSIY.

The TGA measurement shows that HAKSIY is sensitive to the removal of guest solvent molecules, therefore the activation of this structure had to be done over 2 days in a very slow and step-wise temperature increase, in order to avoid its collapse. Overall, HAKSIY is stable up to approximately 400 °C, until which the solvent removal occurs at a constant rate.

The N_2 adsorption isotherm at 77 K and 1 bar (Figure 3.3) was collected to determine the pore volume of the structure, which was found to be 0.190 cm^3/g, approximately 2.8 fold lower than the computational calculated value.

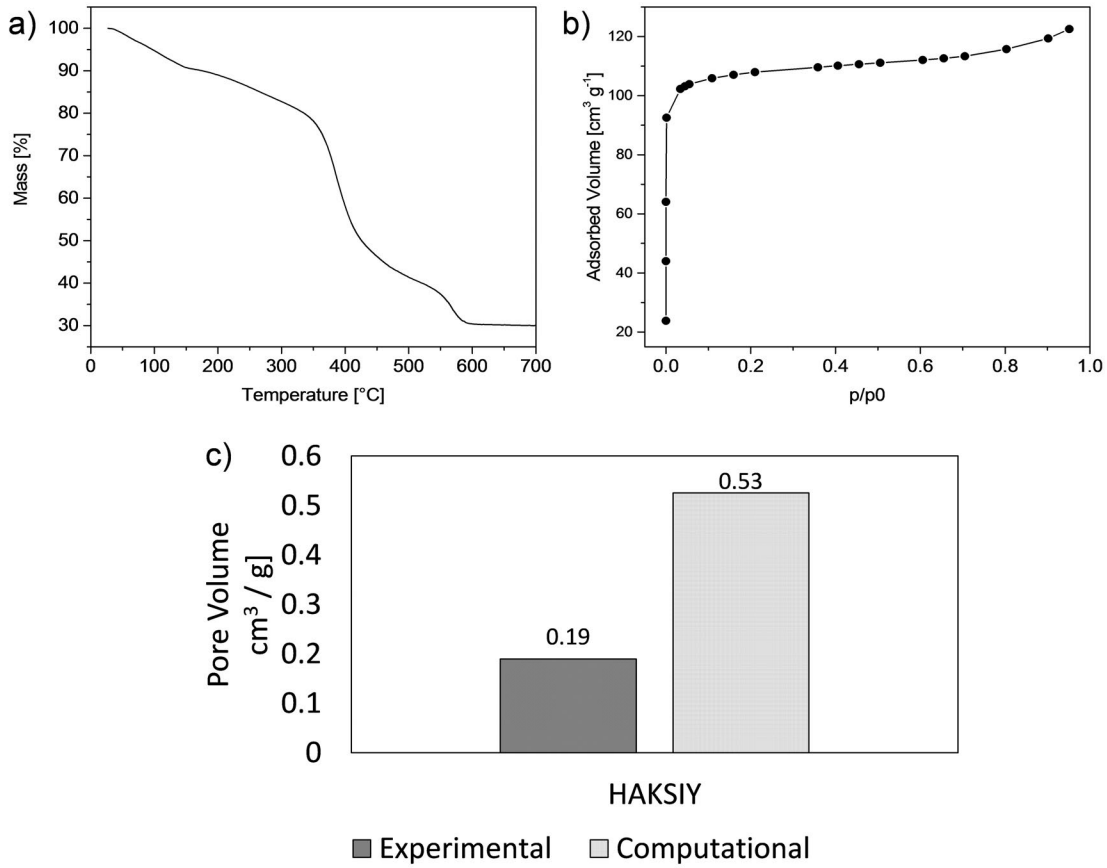

Figure 3.3 – a) TGA, b) N_2 isotherm (collected at 77 K) and c) pore volume measurement of HAKSIY.

Morphological Characteristics. SEM images of HAKSIY were taken (Figure 3.4) to investigate the morphology of the MOF crystals. From Figure 3.4 a), the non-homogeneity of the crystals can be observed.

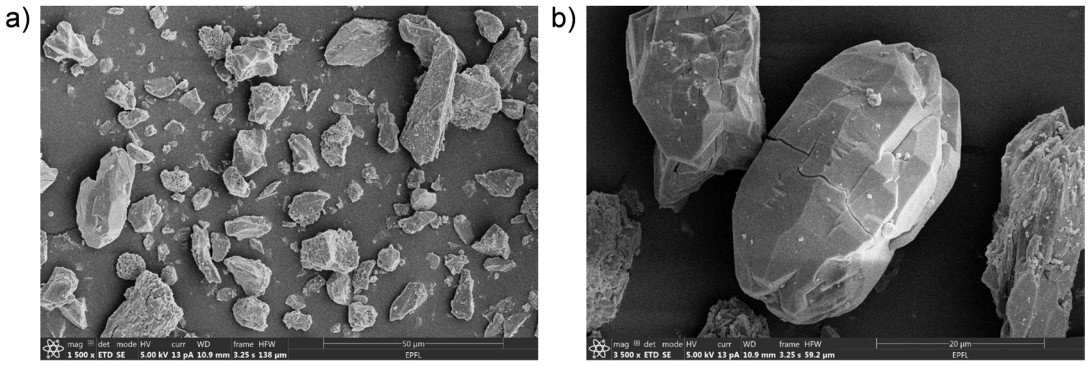

Figure 3.4 – SEM images of HAKSIY at a) 1 500 x and b) 3 500 x magnifications.

Sorption Study. The CO_2 and N_2 experimental adsorption isotherms are not in good agreement with the computationally derived curves (Figure 3.5). At 1.2 bar, the computational results show a CO_2 uptake 10 times higher than the experimental one, while for N_2, it is 8 times higher. Given the large discrepancies and considering the sensitiveness of the MOF to solvent guest molecules removal, it is possible that the activation was not sufficient to clear the pores and active sites completely, lowering the CO_2 adsorption capacity of this structure tremendously when tested in the laboratory.

The computational exploration of more MOF structures is still under progress in order to suggest new promising candidates for CO_2 and N_2 adsorption capacities. As yet, the selected MOFs among the ones that have been suggested have suffered from either synthetic reproducibility or the theraml stability of the structures. Therefore, it can be expected that with the increasing number of promising MOFs that are proposed by calculations, the experimental investigation can find and synthesize promising candidates for wet fuel gas separation.

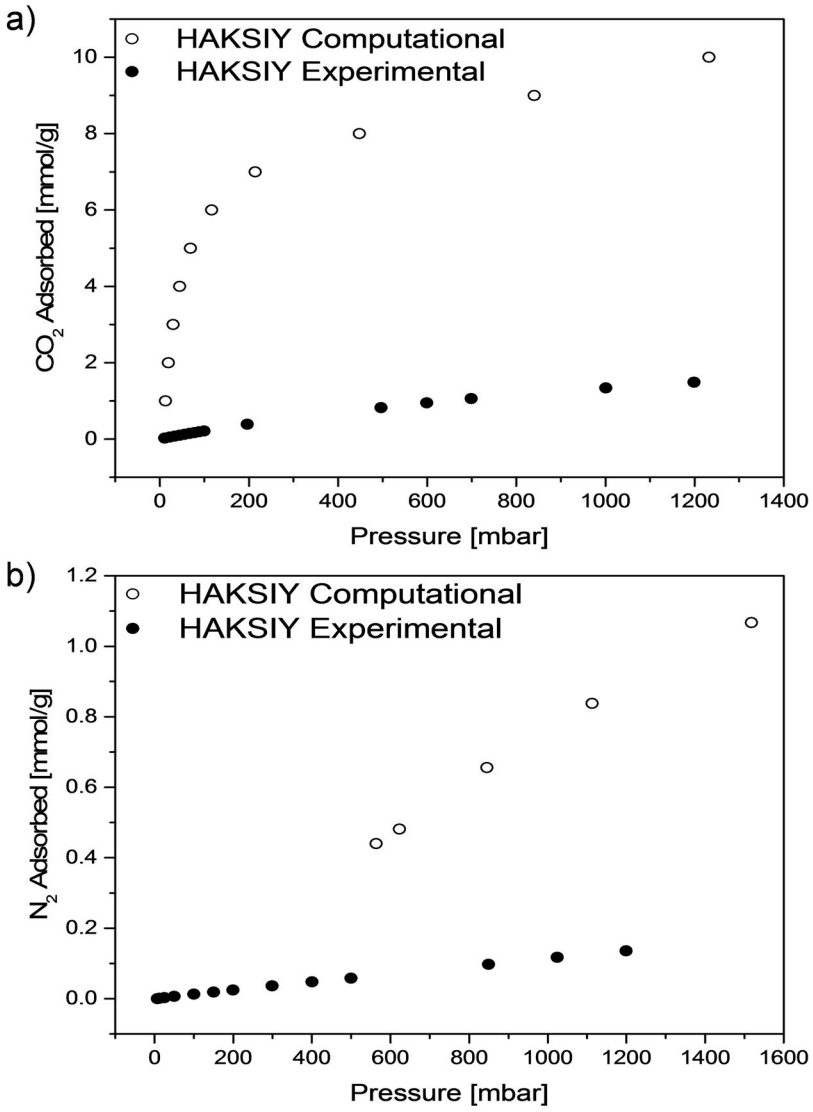

Figure 3.5 – a) CO_2 and b) N_2 experimental (filled) and computationally predicted (empty) adsorption isotherms of HAKSIY.

4 Conclusions & Future/Ongoing Work

Within the scope of this master thesis, we aimed at investigating metal-organic frameworks (MOFs) for carbon capture. MOFs are novel porous materials which can be formed upon the assembly of organic linker(s) and metal components in a 1-, 2- or 3-dimensional periodic network. Thanks to their remarkable structural and functional tunability, these materials have shown promising performances for CO_2 capture, which were here studied further in detail.

In the first section of this thesis, we focused on the current technologies being used for capturing CO_2. In Chapter 2, we focused on elucidating the parameters that possibly affect the CO_2 adsorption uptake. In the first part, isostructural pyrene-based MOFs with different metals (M-TBAPy MOFs, where M = Al, Ga, In and Sc) were studied to assess the influence of the metal on the adsorption capacity. The metal ions in these structures were found to be affecting the inter-aromatic distance between pyrene aromatic rings. Since this position corresponds to the preferential binding site of CO_2, different metals lead to different MOF - CO_2 interactions. The ideal distance for an optimal CO_2 adsorption ranges between 6.5 - 7.0 Å, which was proven to be achieved by using Al(III) as the metal. The remaining structures, which present higher inter-aromatic distances, showed a lower CO_2 uptake, as predicted by the calculations. Discrepancies between the experimental and computational isotherms were observed, which may be due to the assumption of a perfect crystalline structure while computing the isotherms. Ga-TBAPy may undergo a structural distortion upon desolvation similarly to what was observed for In-TBAPy, for which a further investigation is needed.

In the second part of this chapter, another class of pyrene-based MOFs was designed to assess the influence of the topology on the CO_2 uptake. These structures possess the same metal (Zn) and ligand (TBAPy); however, they present different topologies, meaning the formation of different nets with different pore sizes and shapes. These MOFs showed interesting performances with different trends, at lower and higher pressures. This study showed that MOFs can create unique environments by the arrangement of organic linkers surrounding the metal node, which can play an important role in the CO_2 uptake. It was found that the interactions between the CO_2 and MOF are more crucial at lower pressure adsorption, whereas at higher CO_2 loadings, the pore volume becomes more dominant. Moreover, smaller pore size allowed

for stronger interactions between the network and CO_2, facilitating its adsorption compared to a structure possessing larger pore sizes.

In order to take advantage of the academic knowledge to contribute to a more sustainable future, it is of crucial importance to study the application of MOF structures also at an industrial scale. In Chapter 3, we tried to bridge the academic knowledge to industry. Prior to this study, preliminary process simulations were performed to assess the requirements of the process. The screening of thousand of MOFs was performed in order to identify the most promising structures for wet fuel gas applications. From these candidates, only four structures were synthesized in the framework of this study, based on different synthetic criteria (e.g. less complex reaction conditions, commercial availability of the ligands, and low cost of reaction elements). Two structures were successfully synthesized: HAKSIY and EKOPEA. The remaining structures were not reproducible, while EKOPEA was not stable upon activation and collapsed after the removal of guest molecules. This study underlined the importance of screening for large databases in order to select the top performing structures. It is however of crucial importance to have as many promising structures as possible, considering that several MOFs may not be reproducible due to a complex synthesis, or they may be unstable upon exposure to air, solvent addition/removal, etc. Moreover, the CO_2 isotherms of HAKSIY differed highly with the computational predictions. Considering that simulations assume a perfect crystal structure, it may not be trivial to estimate the "error" between experimental and computational isotherms which underlines once more the importance of having several promising MOFs structures to be synthesized.

This work resulted in the understanding and application driven design of MOFs for CO_2 capture. As a future study, the more detailed computational and experimental work on Ga-TBPAy should be performed to understand the structural changes occuring in the MOF. For the anionic structures, Zn-(Ade)(TBAPy) 1 and Zn-(6BA)(TBAPy) 2, single crystal PXRD measurement should be performed to assess the exact positions of the cations and the CO_2 molecules in the pores. The accuracy and thus comparability of simulations can be improved by modelling the cations as freely movable in the pores.

A An appendix

Table A.1 – Elemental analysis of Ga- and Sc-TBAPy.

Element [%]	Ga-TBAPy		Sc-TBAPy	
	Theory	**Experimental**	**Theory**	**Experimental**
C	61.73	59.93	65.52	65.54
H	3.30	3.17	3.50	3.50
N	0	0.08	0	0.07

Table A.2 – Binding energies for all M-TBAPy MOFs (with M = Al, Ga, In and Sc) determined through Density Functional Theory (DFT) and Force Field (FF) calculations.

Structure	Binding Energies [kJ/mol]	
	DFT	**FF**
Al-TBAPy	-32.66	-32.10
Ga-TBAPy	-23.96	-31.89
In-TBAPy	-31.52	-32.00
Sc-TBAPy	-30.42	-30.42

Bibliography

[1] S. Rao and K. Riahi, "The role of non-co2 greenhouse gases in climate change mitigation: long-term scenarios for the 21st century," *The Energy Journal*, no. Special Issue# 3, 2006.

[2] D. W. Kweku, O. Bismark, A. Maxwell, K. A. Desmond, K. B. Danso, E. A. Oti-Mensah, A. T. Quachie, and B. B. Adormaa, "Greenhouse effect: greenhouse gases and their impact on global warming," *Journal of Scientific research and reports*, pp. 1–9, 2017.

[3] L. C. Lau, K. T. Lee, and A. R. Mohamed, "Global warming mitigation and renewable energy policy development from the kyoto protocol to the copenhagen accord—a comment," *Renewable and Sustainable Energy Reviews*, vol. 16, no. 7, pp. 5280–5284, 2012.

[4] L. Hughes, "Biological consequences of global warming: is the signal already apparent?" *Trends in ecology & evolution*, vol. 15, no. 2, pp. 56–61, 2000.

[5] H. Mohajan, "The first industrial revolution: creation of a new global human era," 2019.

[6] E. E. Agency, *Global monitoring laboratory, earth system research laboratories*, https://www.eea.europa.eu/data-and-maps/daviz/contribution-of-the-different-ghgs-5#tab-dashboard-01, 2021.

[7] A. Raza, R. Gholami, R. Rezaee, V. Rasouli, and M. Rabiei, "Significant aspects of carbon capture and storage–a review," *Petroleum*, vol. 5, no. 4, pp. 335–340, 2019.

[8] C. D. Keeling, "Climate change and carbon dioxide: an introduction," *Proceedings of the National Academy of Sciences*, vol. 94, no. 16, pp. 8273–8274, 1997.

[9] H. Zhang, B. J. Bucior, and R. Q. Snurr, "Molecular modeling of carbon dioxide adsorption in metal-organic frameworks," in *Modelling and Simulation in the Science of Micro-and Meso-Porous Materials*, Elsevier, 2018, pp. 99–149.

[10] B. Lv, B. Guo, Z. Zhou, and G. Jing, "Mechanisms of co2 capture into monoethanolamine solution with different co2 loading during the absorption/desorption processes," *Environmental science & technology*, vol. 49, no. 17, pp. 10 728–10 735, 2015.

[11] S. Fawzy, A. I. Osman, J. Doran, and D. W. Rooney, "Strategies for mitigation of climate change: a review," *Environmental Chemistry Letters*, pp. 1–26, 2020.

[12] V. Romanov, "Erratum to: greenhouse gases and clay minerals," in *Greenhouse Gases and Clay Minerals*, Springer, 2018, E1–E1.

[13] M. L. Observatory, *Global monitoring laboratory, earth system research laboratories*, https://gml.noaa.gov/ccgg/trends/, 2021.

[14] B. Sreenivasulu, D. Gayatri, I. Sreedhar, and K. Raghavan, "A journey into the process and engineering aspects of carbon capture technologies," *Renewable and Sustainable Energy Reviews*, vol. 41, pp. 1324–1350, 2015.

[15] T. Wilberforce, A. Olabi, E. T. Sayed, K. Elsaid, and M. A. Abdelkareem, "Progress in carbon capture technologies," *Science of The Total Environment*, p. 143 203, 2020.

[16] B. Smit, J. A. Reimer, C. M. Oldenburg, and I. C. Bourg, *Introduction to carbon capture and sequestration*, 2014.

[17] P. G. Boyd, A. Chidambaram, E. Garcıa-Dıez, C. P. Ireland, T. D. Daff, R. Bounds, A. Gładysiak, P. Schouwink, S. M. Moosavi, M. M. Maroto-Valer, *et al.*, "Data-driven design of metal-organic frameworks for wet flue gas co 2 capture," *Nature*, vol. 576, no. 7786, pp. 253–256, 2019.

[18] M. Bui, C. S. Adjiman, A. Bardow, E. J. Anthony, A. Boston, S. Brown, P. S. Fennell, S. Fuss, A. Galindo, L. A. Hackett, *et al.*, "Carbon capture and storage (ccs): the way forward," *Energy & Environmental Science*, vol. 11, no. 5, pp. 1062–1176, 2018.

[19] R. Ben-Mansour, M. Habib, O. Bamidele, M. Basha, N. Qasem, A. Peedikakkal, T. Laoui, and M. Ali, "Carbon capture by physical adsorption: materials, experimental investigations and numerical modeling and simulations–a review," *Applied Energy*, vol. 161, pp. 225–255, 2016.

[20] B. Han, C. Zhou, J. Wu, D. J. Tempel, and H. Cheng, "Understanding co2 capture mechanisms in aqueous monoethanolamine via first principles simulations," *The Journal of Physical Chemistry Letters*, vol. 2, no. 6, pp. 522–526, 2011.

[21] K. Li, W. Leigh, P. Feron, H. Yu, and M. Tade, "Systematic study of aqueous monoethanolamine (mea)-based co2 capture process: techno-economic assessment of the mea process and its improvements," *Applied Energy*, vol. 165, pp. 648–659, 2016.

[22] G. T. Rochelle, "Amine scrubbing for co2 capture," *Science*, vol. 325, no. 5948, pp. 1652–1654, 2009.

[23] D. M. D'Alessandro, B. Smit, and J. R. Long, "Carbon dioxide capture: prospects for new materials," *Angewandte Chemie International Edition*, vol. 49, no. 35, pp. 6058–6082, 2010.

[24] M. K. Mondal, H. K. Balsora, and P. Varshney, "Progress and trends in co2 capture/separation technologies: a review," *Energy*, vol. 46, no. 1, pp. 431–441, 2012.

[25] S. Gangarapu, A. T. Marcelis, and H. Zuilhof, "Carbamate stabilities of sterically hindered amines from quantum chemical methods: relevance for co2 capture," *ChemPhysChem*, vol. 14, no. 17, pp. 3936–3943, 2013.

[26] J. D. Figueroa, T. Fout, S. Plasynski, H. McIlvried, and R. D. Srivastava, "Advances in co2 capture technology—the us department of energy's carbon sequestration program," *International journal of greenhouse gas control*, vol. 2, no. 1, pp. 9–20, 2008.

[27] M. Martın, "Carbon capture, how and then what," *J. Adv. Chem. Eng*, vol. 4, e102, 2014.

[28] Y. Tao, H. Kanoh, L. Abrams, and K. Kaneko, "Mesopore-modified zeolites: preparation, characterization, and applications," *Chemical reviews*, vol. 106, no. 3, pp. 896–910, 2006.

[29] C. Lu, H. Bai, B. Wu, F. Su, and J. F. Hwang, "Comparative study of co2 capture by carbon nanotubes, activated carbons, and zeolites," *Energy & Fuels*, vol. 22, no. 5, pp. 3050–3056, 2008.

[30] F. P. Kinik, S. Kampouri, F. M. Ebrahim, B. Valizadeh, and K. C. Stylianou, "Porous metal-organic frameworks for advanced applications," 2020.

[31] C. Singh, S. Mukhopadhyay, and I. Hod, "Metal–organic framework derived nanomaterials for electrocatalysis: recent developments for co 2 and n 2 reduction," *Nano Convergence*, vol. 8, no. 1, pp. 1–10, 2021.

[32] R. Poloni, K. Lee, R. F. Berger, B. Smit, and J. B. Neaton, "Understanding trends in co2 adsorption in metal–organic frameworks with open-metal sites," *The journal of physical chemistry letters*, vol. 5, no. 5, pp. 861–865, 2014.

[33] Ü. Kökçam-Demir, A. Goldman, L. Esrafili, M. Gharib, A. Morsali, O. Weingart, and C. Janiak, "Coordinatively unsaturated metal sites (open metal sites) in metal–organic frameworks: design and applications," *Chemical Society Reviews*, vol. 49, no. 9, pp. 2751–2798, 2020.

[34] J. S. Costa, P. Gamez, C. A. Black, O. Roubeau, S. J. Teat, and J. Reedijk, *Chemical modification of a bridging ligand inside a metal–organic framework while maintaining the 3d structure*, 2008.

[35] M. Alhamami, H. Doan, and C.-H. Cheng, "A review on breathing behaviors of metal-organic-frameworks (mofs) for gas adsorption," *Materials*, vol. 7, no. 4, pp. 3198–3250, 2014.

[36] O. K. Farha and J. T. Hupp, "Rational design, synthesis, purification, and activation of metal- organic framework materials," *Accounts of chemical research*, vol. 43, no. 8, pp. 1166–1175, 2010.

[37] P. Cruz, J. Santos, F. Magalhaes, and A. Mendes, "Cyclic adsorption separation processes: analysis strategy and optimization procedure," *Chemical Engineering Science*, vol. 58, no. 14, pp. 3143–3158, 2003.

[38] F. P. Kinik, A. Ortega-Guerrero, D. Ongari, C. P. Ireland, and B. Smit, "Pyrene-based metal organic frameworks: from synthesis to applications," *Chemical Society Reviews*, 2021.

[39] D. Zych, "Non-k region disubstituted pyrenes (1, 3-, 1, 6-and 1, 8-) by (hetero) aryl groups," *Molecules*, vol. 24, no. 14, p. 2551, 2019.

[40] S. L. Anderson, P. G. Boyd, A. Gładysiak, T. N. Nguyen, R. G. Palgrave, D. Kubicki, L. Emsley, D. Bradshaw, M. J. Rosseinsky, B. Smit, *et al.*, "Nucleobase pairing and photodimerization in a biologically derived metal-organic framework nanoreactor," *Nature communications*, vol. 10, no. 1, pp. 1–8, 2019.

[41] Y.-L. Huang, P.-L. Qiu, J.-P. Bai, D. Luo, W. Lu, and D. Li, "Exclusive recognition of acetone in a luminescent biomof through multiple hydrogen-bonding interactions," *Inorganic chemistry*, vol. 58, no. 12, pp. 7667–7671, 2019.

[42] K. C. Stylianou, J. Rabone, S. Y. Chong, R. Heck, J. Armstrong, P. V. Wiper, K. E. Jelfs, S. Zlatogorsky, J. Bacsa, A. G. McLennan, *et al.*, "Dimensionality transformation through paddlewheel reconfiguration in a flexible and porous zn-based metal–organic framework," *Journal of the American Chemical Society*, vol. 134, no. 50, pp. 20 466–20 478, 2012.

[43] R. Seetharaj, P. Vandana, P. Arya, and S. Mathew, "Dependence of solvents, ph, molar ratio and temperature in tuning metal organic framework architecture," *Arabian journal of chemistry*, vol. 12, no. 3, pp. 295–315, 2019.

[44] T. C. Wang, N. A. Vermeulen, I. S. Kim, A. B. Martinson, J. F. Stoddart, J. T. Hupp, and O. K. Farha, "Scalable synthesis and post-modification of a mesoporous metal-organic framework called nu-1000," *Nature protocols*, vol. 11, no. 1, pp. 149–162, 2016.

[45] K. C. Stylianou, R. Heck, S. Y. Chong, J. Bacsa, J. T. Jones, Y. Z. Khimyak, D. Bradshaw, and M. J. Rosseinsky, "A guest-responsive fluorescent 3d microporous metal- organic framework derived from a long-lifetime pyrene core," *Journal of the American Chemical Society*, vol. 132, no. 12, pp. 4119–4130, 2010.

[46] D. Ongari, P. G. Boyd, S. Barthel, M. Witman, M. Haranczyk, and B. Smit, "Accurate characterization of the pore volume in microporous crystalline materials," *Langmuir*, vol. 33, no. 51, pp. 14 529–14 538, 2017.

[47] Z. Wang, W. Qiu, Y. Yang, and C. Liu, "Atomic-size and lattice-distortion effects in newly developed high-entropy alloys with multiple principal elements," *Intermetallics*, vol. 64, pp. 63–69, 2015.

[48] Z. Li, P. Liu, C. Ou, and X. Dong, "Porous metal–organic frameworks for carbon dioxide adsorption and separation at low pressure," *ACS Sustainable Chemistry & Engineering*, vol. 8, no. 41, pp. 15 378–15 404, 2020.

[49] P. Silva, S. M. Vilela, J. P. Tomé, and F. A. A. Paz, "Multifunctional metal–organic frameworks: from academia to industrial applications," *Chemical Society Reviews*, vol. 44, no. 19, pp. 6774–6803, 2015.

[50] *Prisma - act programme - accelerating ccs technologies*, https://prisma.hw.ac.uk/, Accessed: 07.06.2021.

[51] D. Ongari, A. V. Yakutovich, L. Talirz, and B. Smit, "Building a consistent and reproducible database for adsorption evaluation in covalent–organic frameworks," *ACS central science*, vol. 5, no. 10, pp. 1663–1675, 2019.

[52] X.-Y. Hou, X. Wang, F. Fu, J.-J. Wang, and L. Tang, "Synthesis and characterization of two- and three-dimensional coordination polymers built with 3, 5-bis (4-carboxy-phenyl)-1, 2, 4-triazole and/or 1, 4-bis (imidazol-1-ylmethyl) benzene," *Journal of Coordination Chemistry*, vol. 66, no. 17, pp. 3126–3136, 2013.

[53] R. Jones, J. Thomas, J. Chen, R. Xu, Q. Huo, S. Li, Z. Ma, and A. Chippindale, "Structure of an unusual aluminium phosphate ([al [sub 5] p [sub 6] o [sub 24] h][sup 2 [minus]] 2 [n (c [sub 2] h [sub 5])[sub 3] h][sup+][center dot] 2h [sub 2] o) jdf-20 with large elliptical apertures," *Journal of Solid State Chemistry;(United States)*, vol. 102, no. 1, 1993.

[54] X. Zhao, X. Bu, E. T. Nguyen, Q.-G. Zhai, C. Mao, and P. Feng, "Multivariable modular design of pore space partition," *Journal of the American Chemical Society*, vol. 138, no. 46, pp. 15 102–15 105, 2016.

[55] W. Zheng, Y. Wei, X. Xiao, and K. Wu, "Spontaneous asymmetric crystallization of a quartz-type framework from achiral precursors," *Dalton Transactions*, vol. 41, no. 11, pp. 3138–3140, 2012.

[56] C. Pettinari, A. Tabacaru, I. Boldog, K. V. Domasevitch, S. Galli, and N. Masciocchi, "Novel coordination frameworks incorporating the 4, 4-bipyrazolyl ditopic ligand," *Inorganic chemistry*, vol. 51, no. 9, pp. 5235–5245, 2012.

[57] L. Zhai, W.-W. Zhang, J.-L. Zuo, and X.-M. Ren, "Simultaneous observation of ligand-based fluorescence and phosphorescence within a magnesium-based cp/mof at room temperature," *Dalton Transactions*, vol. 45, no. 30, pp. 11 935–11 938, 2016.

[58] J.-X. Yang, Y.-Y. Qin, R.-P. Ye, X. Zhang, and Y.-G. Yao, "Employing mixed-ligand strategy to construct a series of luminescent cd (ii) compounds with structural diversities," *CrystEngComm*, vol. 18, no. 42, pp. 8309–8320, 2016.

[59] J.-D. Lin, S.-T. Wu, Z.-H. Li, and S.-W. Du, "Syntheses, topological analyses, and nlo-active properties of new cd (ii)/m (ii)(m= ca, sr) metal–organic frameworks based on r-isophthalic acids (r= h, oh, and t-bu)," *Dalton Transactions*, vol. 39, no. 44, pp. 10 719–10 728, 2010.

[60] F. A. Almeida Paz, F.-N. Shi, T. Trindade, J. Rocha, and J. Klinowski, "Catena-[1, 3-diammoniopropane di-μ2-hydroxo-di-μ4-phosphato-trioxotrivanadium dihydrate]: a redetermination at 180 (2) k," *Acta Crystallographica Section E: Structure Reports Online*, vol. 59, no. 4, pp. m179–m182, 2003.

[61] R. Podgajny, D. Pinkowicz, T. Korzeniak, W. Nitek, M. Rams, and B. Sieklucka, "High t c ferrimagnetic organic- inorganic hybrid materials with mnii- l- mnii and mnii- nc-nbiv linkages (l= pyrazine, pyrazine-n, n '-dioxide, bipyrimidine)," *Inorganic chemistry*, vol. 46, no. 24, pp. 10 416–10 425, 2007.

[62] Y.-L. Hou, G. Xiong, B. Shen, B. Zhao, Z. Chen, and J.-Z. Cui, "Structures, luminescent and magnetic properties of six lanthanide–organic frameworks: observation of slow magnetic relaxation behavior in the dy iii compound," *Dalton Transactions*, vol. 42, no. 10, pp. 3587–3596, 2013.

[63] J. Zhang, S. Chen, A. Zingiryan, and X. Bu, "Integrated molecular chirality, absolute helicity, and intrinsic chiral topology in three-dimensional open-framework materials," *Journal of the American Chemical Society*, vol. 130, no. 51, pp. 17 246–17 247, 2008.

[64] Y. Zhao, D. J. Guo, B. Y. Su, and S.-Y. Xie, "Crystal structure of poly [triaqua-μ2-sulfato-κ4o, o': o", o"'-pyridine-3, 5-dicarboxylato-κ4o, o': o": o"'] cerium (iii) monohydrate, c7h11ceno10s," *Zeitschrift für Kristallographie-New Crystal Structures*, vol. 228, no. 3, pp. 359–360, 2013.

[65] S.-Q. Guo, D. Tian, X. Zheng, and H. Zhang, "A (3, 4, 10)-connected 3d sandwich-type metal-organic framework with trinuclear zinc (ii) cluster and two kinds of discrete zinc (ii) ions," *Inorganic Chemistry Communications*, vol. 14, no. 12, pp. 1876–1879, 2011.

[66] P. Lama, H. Aggarwal, C. X. Bezuidenhout, and L. J. Barbour, "Giant hysteretic sorption of co2: in situ crystallographic visualization of guest binding within a breathing framework at 298 k," *Angewandte Chemie International Edition*, vol. 55, no. 42, pp. 13 271–13 275, 2016.